



UvA-DARE (Digital Academic Repository)

Ferrocene-based light-responsive carbon nano hoops

Kręcijasz, R.B.

Publication date
2026

[Link to publication](#)

Citation for published version (APA):

Kręcijasz, R. B. (2026). *Ferrocene-based light-responsive carbon nano hoops*. [Thesis, fully internal, Universiteit van Amsterdam].

General rights

It is not permitted to download or to forward/distribute the text or part of it without the consent of the author(s) and/or copyright holder(s), other than for strictly personal, individual use, unless the work is under an open content license (like Creative Commons).

Disclaimer/Complaints regulations

If you believe that digital publication of certain material infringes any of your rights or (privacy) interests, please let the Library know, stating your reasons. In case of a legitimate complaint, the Library will make the material inaccessible and/or remove it from the website. Please Ask the Library: <https://uba.uva.nl/en/contact>, or a letter to: Library of the University of Amsterdam, Secretariat, P.O. Box 19185, 1000 GD Amsterdam, The Netherlands. You will be contacted as soon as possible.

4

Size-Dependent Properties of Ferrocene[n]cycloparaphenylenes ($n = 6-8$)

Abstract

We report the synthesis and comprehensive characterization of a series of strained ferrocene-cycloparaphenylene macrocycles, Fc[*n*]CPPs (*n* = 6–8), as photoactivable Fe²⁺ carriers. Structural, spectroscopic, electrochemical, and computational analyses across the series reveal how hoop strain modulates the geometry and photoreactivity of the Fc center. Notably, efficient Fe–Cp bond dissociation occurs even in less distorted systems, suggesting that strain-induced kinetic effect—and not just structural distortion of the metallocene—drives photoreactivity. Our findings highlight the tunability of CPP strain to modulate Fe²⁺ uncaging and provide new insights into the structure–reactivity relationship in ferrocene chemistry. These results are encouraging for future advancements in organometallic and supramolecular chemistry, as well as biomedical applications.

4.1 Introduction

The popularity of ferrocene (**Fc**), discovered in the early 1950s,^[1] can be attributed to its exceptional properties, such as a high solubility in common organic solvents, redox-active behavior and sandwich-like structure allowing for rotational fluxionality. Moreover, **Fc** displays a high chemical stability with the bond dissociation energy (BDE) of the iron–cyclopentadienyl (Fe–Cp) bond of ~90 kcal/mol,^[2] comparable to strong C–C bonds. Owing to the unique combination of these properties, **Fc** has become a highly valuable compound in various fields including catalysis,^[3–5] sensing,^[6–8] materials science,^[9–11] molecular electronics^[12,13] and medicine.^[14,15] While its stability is advantageous, the rupture of the Fe–Cp bond in **Fc** opens new avenues for reactivity. This becomes feasible in strained systems such as ferrocenophanes, where short bridges of one or two atoms between the Cp rings introduce ring strain ($E_{\text{strain}} = 14\text{--}31 \text{ kcal mol}^{-1}$), promoting Fe–Cp bond dissociation.^[16–19] Pioneered by Manners, these systems have enabled light-triggered ring-opening polymerizations to generate functional metallapolymers.^[20–23] More recently, **Fc** has been explored as a mechanophore—a mechanically responsive unit—capable of Fe–Cp bond rupture under force generated by ultrasound.^[24–26] Notably, the mechanical strength of this bond was found to be comparable to that of the C–N bond of azobisdialkyl nitrile (BDE < 30 kcal mol⁻¹).^[25]

Embedding **Fc** into polymer backbones thus enables force-induced iron release, a feature with promising implications because iron plays a fundamental role in many biological processes^[27] owing to its versatile redox chemistry and ability to coordinate various ligands. For example, iron serves as cofactor in electron transfer reactions^[28,29] and redox metabolism,^[30] and is an essential component of heme and iron-sulfur clusters, which play critical roles in the function of hemoglobin,^[31] myoglobin,^[32] cytochromes,^[33] and a variety of enzymes involved in respiration^[34] and DNA synthesis.^[35] Iron acquisition, transport, storage, and overall homeostasis are thus critical,^[36,37] and both iron deficiency and overload can induce pathological conditions.^[38,39] Given the fundamental role of iron in biological processes, development of new molecular tools that permit precise and efficient mechanical activation of iron is of high interest.

Recently, we introduced ferrocene–cycloparaphenylene **Fc[6]CPP** (Figure 4.1) as an unprecedented macrocyclic photocage capable of releasing Fe²⁺ ions upon green light activation with Fc serving as the iron carrier.^[40] The incorporation of this metallocene into the backbone of the strained π -conjugated [*n*]cycloparaphenylene^[41,42] led to structural distortion of Fc as a result of the large strain in the macrocyclic nano hoop, similar to the effect of mechanical stress on Fc. This distortion appears to promote photoinduced dissociation of the iron–cyclopentadienyl (Fe–Cp) bond like in the smaller, but significantly more distorted Fc systems, such as [*n*]ferrocenophanes,^[21,22,43] making **Fc[6]CPP** >1000-fold more efficient compared to **Fc**

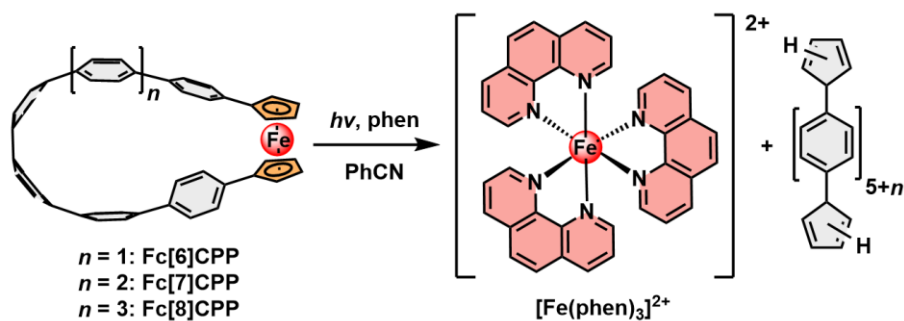


Figure 4.1. Photoreactivity of ferrocene-based π -conjugated macrocycles described in this work.

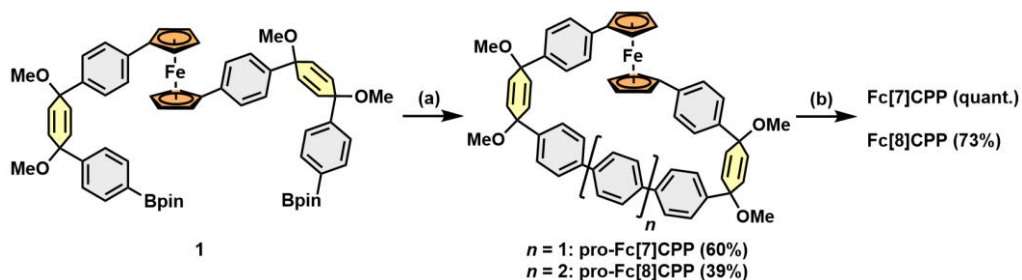
itself.^[21,22,43] The ability to trigger the Fe^{2+} ions release from **Fc[6]CPP** in water-rich solvent mixtures suggests that this strategy might serve as a tool for photochemical regulation of iron levels at physiological conditions. The possibility to fine-tune the strain in CPPs by altering the number of *para*-phenylenes in the macrocycle could offer a handle to modulate the properties and photochemical reactivity of such photocages and help understand the underlying Fe–Cp photodissociation mechanism. It is currently unclear whether the observed photoreactivity of Fc is exclusive to **Fc[6]CPP** and the significantly more distorted and strained $[n]$ ferrocenophanes. Otherwise, photochemical de-coordination from structurally unperturbed Fc can only be achieved with highly electron-deficient, weakly coordinating perfluorinated Cp ligands.^[44,45] It is therefore anticipated that smaller Fc distortion in larger, less strained Fc $[n]$ CPP systems ($n > 6$) with strongly coordinating Cp's will diminish the photochemical reactivity and the efficient release of Fe^{2+} .

In this work, we complete and investigate the series of Fc $[n]$ CPP ($n = 6–8$) to establish structure–property relationships as a function of strain in these nano hoops by analysing their single-crystal X-ray diffraction, UV–vis, electrochemical, and computational data, and photochemical reactivity. Thereby we demonstrate that distorting the structure of Fc is not necessary to efficiently photodissociate the Cp ligand and to release the iron cargo. We explain this unexpected outcome by a kinetic effect that offsets the strong coordination of Cp's, an effect determined by the strain localized in the curved hoop-like ligands that serve as a source of internal mechanical stress. Therefore, Fc $[n]$ CPPs represent a new family of photoactive metallocene macrocycles that allow for fine-tuning the uncaging efficiency by controlling the strain in the ligands, without the need for extensive distortion of the metallocene. Our work thus provides important insights into the drivers of photochemical reactivity of metallocenes and will stimulate development of new photo(mechano)active molecular systems for a wide range of applications.

4.2 Results and Discussion

To study the relationship between the strain and the properties of **Fc[n]CPPs**, we aimed to prepare a series ($n = 6-8$) where the strain is expected to gradually decrease with increasing n , i.e., the number of phenylenes in the macrocycle. Our initial computational investigation estimated that the largest member of this series, namely **Fc[8]CPP**, would already display a subtle distortion of the ferrocene structure. The **Fc[6]CPP** was synthesized via **pro-Fc[6]CPP** as reported previously from building block **1** (Scheme 4.1).^[40] The nanohoop **Fc[7]CPP** was obtained in two steps from **1**. First, compound **1** was reacted with 1,4-dibromobenzene in the Suzuki cross-coupling reaction providing the pro-aromatic macrocycle **pro-Fc[7]CPP** in 60% yield (Scheme 4.1). Subsequently, the reductive aromatization of the two cyclohexa-2,5-dienyl moieties in **pro-Fc[7]CPP** using SnCl_2/HCl ^[46] proceeded efficiently, affording pure **Fc[7]CPP** in a nearly quantitative yield. The larger nanohoop **Fc[8]CPP** was synthesized following the same route, although lower yields were observed in both the macrocyclization (39%) and the aromatization (73%) steps. Like **Fc[6]CPP**, **Fc[7]CPP** and **Fc[8]CPP** remain chemically stable for several months as a solid under ambient conditions. The solubility decreases with the increasing size of the nanohoop, and both **Fc[7]CPP** and **Fc[8]CPP** exhibited a moderate solubility in common organic solvents such as dichloromethane and tetrahydrofuran. However, they were well soluble in 1,1,2,2-tetrachloroethane. The structures of **pro-Fc[n]CPPs** and **Fc[n]CPPs** ($n = 6-8$) were confirmed by 1D and 2D NMR spectroscopy, along with high-resolution mass spectrometry (HRMS).

Vapor diffusion of cyclohexane into dichloromethane solutions of **Fc[7]CPP** (4 °C) and **Fc[8]CPP** (-20 °C) yielded single crystals suitable for X-ray diffraction (XRD). The XRD data analysis revealed that both nanohoops crystallized in monoclinic $P2_1$ space group. Similar to **Fc[6]CPP**, the fluxionality of the Fc center allowed both nanohoops to adopt an oval shape (Figure 4.2), featuring an elliptical cavity of 13.8 Å in length and 8.1 Å in width for **Fc[7]CPP**, and 15.7 Å in



Scheme 4.1. Synthesis of **Fc[7]CPP** and **Fc[8]CPP**. Reaction conditions: (a) 1,4-dibromobenzene or 4,4'-dibromobiphenyl (1 equiv.), SPhos Pd Gen III (0.1 equiv.), K_3PO_4 (67 equiv.), 1,4-dioxane/ H_2O , 80 °C, 14 h (b) H_2SnCl_4 (3.6 equiv.), THF, RT, 1.5 h.

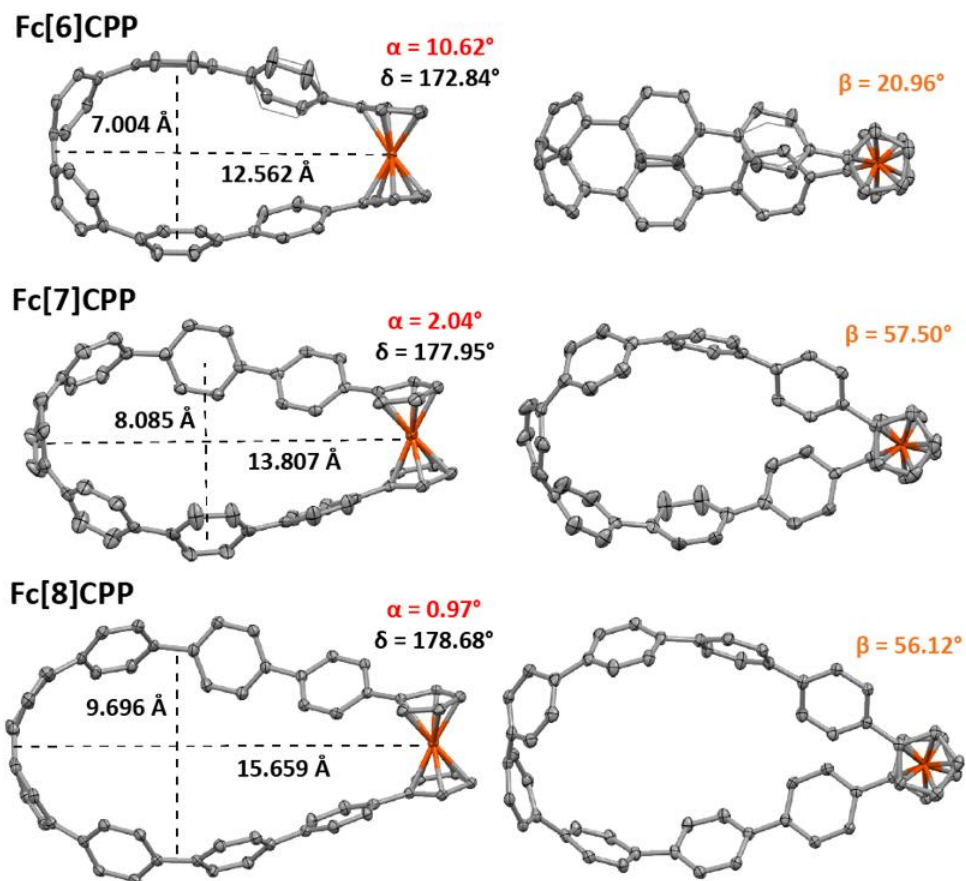


Figure 4.2. X-ray crystal structures of **Fc[*n*]CPPs** ($n = 6-8$). Gray: C, orange: Fe. Thermal ellipsoids shown at 50% probability; all hydrogen atoms and solvent were omitted for clarity.

length and 9.7 Å in width for **Fc[8]CPP**. The access to the crystal structures of all three **Fc[*n*]CPPs** ($n = 6-8$) allows for the comparison of the effect of strain on the Fc geometry distortion defined by (see Figure S4.1, Table 4.1): (i) the tilt angle α between the Cp ring planes, (ii) the angle β describing the extent of rotation between the substituted Cp carbons, and (iii) the Cp–Fe–Cp angle δ . As expected, the smallest nanohoop **Fc[6]CPP** exhibits the most distorted Fc moiety ($\alpha = 10.62^\circ$; $\delta = 172.84^\circ$), while the values determined for **Fc[7]CPP** ($\alpha = 2.04^\circ$; $\delta = 177.95^\circ$) and **Fc[8]CPP** ($\alpha = 0.97^\circ$; $\delta = 178.68^\circ$) differ only slightly from the ideal values in unperturbed, strain-free **Fc** ($\alpha = 0^\circ$; $\delta = 180^\circ$). The extent of Fc distortion correlates with the strain energies calculated for the nanohoops in the series (DFT, Table 4.2). The E_{strain} of 58.0 kcal mol⁻¹ of **Fc[6]CPP** is higher than those obtained for both **Fc[7]CPP** and **Fc[8]CPP** by 8.6 and 13.2 kcal mol⁻¹, respectively. The strain impacts not only the Fc core but also the overall conformation of the nanohoop, as reflected in the varying values of the angle β . While the values of β in **Fc[7]CPP**

Table 4.1. Summary of structural, redox and photophysical properties of **Fc[n]CPPs** ($n = 6-8$).

Compd.	α (°)	β (°)	δ (°)	1 st $E_{1/2}^{a,b}$ (mV)	2 nd $E_{1/2}^{a,b}$ (mV)	$\lambda_{\text{abs,max}}$ 1 st (nm)	$\lambda_{\text{abs,max}}$ 2 nd transition (nm)	$\epsilon^{b,d}$ (10 ³ M ⁻¹ cm ⁻¹)	$\epsilon^{b,e}$ (10 ³ M ⁻¹ cm ⁻¹)	$\phi^{b,f}$ (%)	
										500 equiv. phen	25 equiv, phen
pro- Fc[6]CPP ⁵⁰	1.85	103.24	179.09	–	–	–	–	–	0.9	(4.9 ± 0.4) × 10 ⁻³	–
Fc[6]CPP	10.62	20.96	172.84	-41 ± 11	577 ± 6	470	330	57 ± 3	2.57 ± 0.11	4.3 ± 0.3	0.63 ± 0.14
Fc[7]CPP	2.04	57.50	177.95	-8 ± 6	599 ± 14	455	329	67 ± 2	1.57 ± 0.04	2.4 ± 0.2	0.20 ± 0.04
Fc[8]CPP	0.97	56.12	178.68	1 ± 11	675 ± 6	442	331	74 ± 1	1.42 ± 0.01	1.3 ± 0.1	0.07 ± 0.008

^a Determined by DPV in 0.1 M *n*-Bu₄NPF₆/1,1,2,2-tetrachloroethane with respect to **Fc/Fc⁺**. ^b ± Standard deviation of the mean. ^c Second derivative absorption spectra. ^d At $\lambda_{\text{abs,max}}$ in PhCN. ^e At $\lambda_{\text{abs}} = 472$ nm in PhCN. ^f Quantum yield of [Fe(phen)₃]²⁺ formation in PhCN.

Table 4.2. The calculated^a total (^{tot} E_{strain}) and local strain energies on ferrocene (^{Fc} E_{strain}) and CPP (^{CPP} E_{strain}) fragments in **Fc[n]CPPs** ($n = 6-8$) and the transition state energies (ΔH^\ddagger) of the nucleophilic attack of phen on the Fc unit in triplet **Fc[n]CPPs** ($n = 6-8$) and **Fc**.

Compd.	^{tot} E_{strain} (kcal mol ⁻¹)	^{Fc} E_{strain} (kcal mol ⁻¹)	^{CPP} E_{strain} (kcal mol ⁻¹)	ΔH^\ddagger (kcal mol ⁻¹) ^b
Fc[6]CPP	58.0	2.3	55.6	1.6
Fc[7]CPP	49.4	0.7	50.1	2.2
Fc[8]CPP	44.8	0.7	45.6	4.8
Fc	0.0	0.0	n.a. ^c	10.1

^a Values calculated by wB97XD/cc-pVTZ level of theory on the B3LYP/6-31G(d) optimized structures and Fc or CPP fragments see the SI for the computational details. ^b D3PBE03/cc-pVTZ level of theory on the BP86/6-31G(d) optimized geometries including the unscaled ZPVE correction and empirical dispersion correction (D3, see the SI for further functionals). ^c n.a. = no available.

and **Fc[8]CPP** are similar ($\beta = 57.5$ vs 56.1°), **Fc[6]CPP** shows a significantly lower value $\beta = 21.0^\circ$. As a result, the conformations of **Fc[7]CPP** and **Fc[8]CPP** exhibit an additional twist in the *para*-phenylene segment, not permissible in the more strained **Fc[6]CPP**.

In oval *meta*-CPPs,^[47] one side of the nanohoop suffers from higher dihedral strain than what is found in ring-shaped CPPs,^[48] which translates to lower values of the phenylene–phenylene dihedral angles (CPPs: $\sim 26^\circ$; *m*CPPs: 19°). These dihedral angles in **Fc[6]CPP** (8° – 18°) and, in particular, **Fc[7]CPP** ($<7^\circ$) are very low at the side of the nanohoop opposite to Fc. Such strain must be compensated by increasing the π -MOs overlap, which is expected to localize the corresponding filled MOs to this part of the nanohoop and increase their energy. This is reflected in the electrochemistry of the **Fc[*n*]CPPs** ($n = 6$ – 8) (Figure 4.3, Table 4.1) studied by cyclic voltammetry (CV) and differential pulse voltammetry (DPV) in 1,1,2,2-tetrachloroethane solutions with 0.1 M [*n*-Bu₄N][PF₆] as supporting electrolyte. All three nanohoops possess two anodic waves. The first anodic wave displays a full reversibility as confirmed by the Randles–Ševčík analysis (Figures S4.10–S4.12). The measured half-wave potentials ($E_{1/2}$) deviate only slightly from the **Fc/Fc⁺** couple, which is consistent with the nonbonding HOMO (d_{z^2}) residing on the Fc in the nanohoops. The value of $E_{1/2}$ increases modestly by ca 40 mV with increasing the nanohoop size suggesting that the strain on Fc in **Fc[*n*]CPPs** ($n = 6$ – 8) is not substantial. In contrast, the second anodic wave at 0.6–0.7 V is irreversible for all compounds with a more pronounced shift

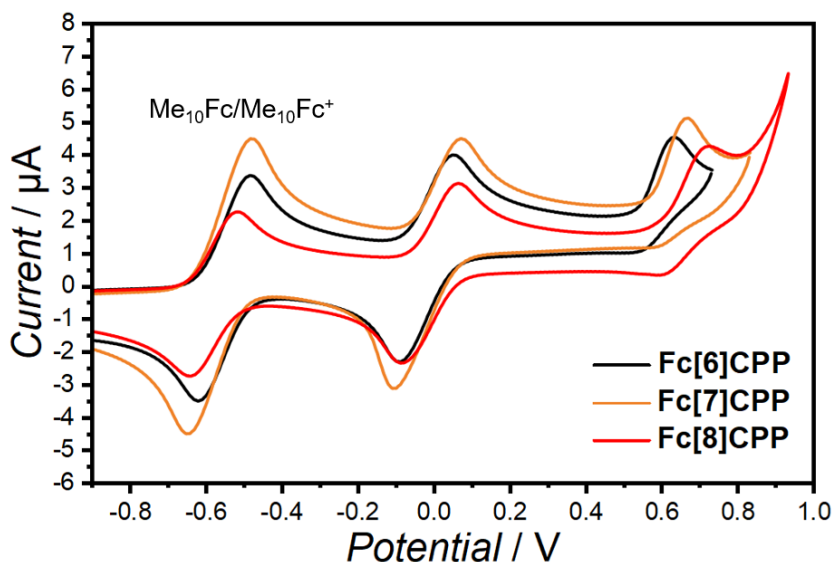


Figure 4.3. Cyclic voltammetry (CV) (scan rate = 100 mV s^{-1}) of **Fc[*n*]CPPs** ($n = 6$ – 8) and decamethylferrocene (Me_{10}Fc) used as internal standard recorded in 0.1 M *n*-Bu₄NPF₆/1,1,2,2-tetrachloroethane. Data referenced vs **Fc/Fc⁺**.

(~100 mV) of the half-wave oxidation potential with the nanohoop size. We assigned this second redox event to the oxidation of the nanohoop moiety. The parent $[n]$ CPPs undergo oxidation that follows a similar size-dependent trend,^[49,50] although the $E_{1/2}$ values observed for **Fc** $[n]$ CPPs ($n = 6-8$) are lower than those reported for the $[n]$ CPPs. In fact, **[10]CPP** ($E_{\text{strain}} = 57.7 \text{ kcal mol}^{-1}$) and **[12]CPP** ($E_{\text{strain}} = 48.1 \text{ kcal mol}^{-1}$) exhibit strain energies^[51] comparable to those of **Fc****[6]CPP** and **Fc****[7]CPP**, yet their reported $E_{1/2}$ values^[52] are significantly higher, reaching 0.74 V and 0.83 V, respectively. Another notable observation is the unexpected increase in the $E_{1/2}$ value from $(0.577 \pm 0.006) \text{ V}$ for **Fc****[6]CPP** to $(0.675 \pm 0.006) \text{ V}$ for **Fc****[8]CPP**, while **Fc****[7]CPP** showed only a minor shift of 22 mV relative to **Fc****[6]CPP**. As reported in the literature,^[53] increasing the size of $[n]$ CPP by one phenylene unit has a more pronounced impact on the oxidation potential in the small, more strained nanohoos compared to the larger, less strained ones. For example, the $E_{1/2}$ increases by >100 mV from **[6]CPP** to **[7]CPP**,^[54-56] but by only ~20 mV between **[12]CPP** and **[13]CPP**.^[52] The unusual behavior observed in the **Fc** $[n]$ CPPs ($n = 6-8$) series is most likely attributable to the large dihedral strain and enhanced MO overlap (*vide supra*).

All **Fc** $[n]$ CPPs ($n = 6-8$) displayed a typical absorption pattern characteristic for $[n]$ CPPs (Figure 4.4a), featuring a strong absorption peak around 330 nm and a separate band at ~400 nm which corresponds to the lowest energy transition localized on the curved *para*-phenylenes. The molar decadic absorption coefficient of the 330 nm transitions increases with the nanohoop size (Table 4.1), in accordance with increasing the size of the π -system and the trend observed in $[n]$ CPPs.^[41,49,57-59] The formally forbidden absorption (>430 nm) arising from the transition localized to the Fc unit is not resolved. Therefore, we applied the first and second derivatives to the absorption spectra (Figure 4.4b, Figure S4.13). Indeed, second-derivative absorption spectra provide clear maxima for the Fc-centered transition in all nanohoos and indicate that the absorption maximum blue-shifts with the increasing nanohoop size corresponding to the widening of the HOMO–LUMO gap. The molar decadic absorption coefficient is the largest for the smallest **Fc****[6]CPP** ($\epsilon_{472 \text{ nm}} = 2570 \text{ M}^{-1} \text{ cm}^{-1}$) and it does not change markedly going from **Fc****[7]CPP** ($1570 \text{ M}^{-1} \text{ cm}^{-1}$) to **Fc****[8]CPP** ($1420 \text{ M}^{-1} \text{ cm}^{-1}$). This agrees well with the extent of structural distortion of Fc, which partially allows the corresponding transition by lifting the symmetry on Fc. Indeed, symmetric **Fc** itself exhibits a “forbidden” transition with significantly lower $\epsilon_{472 \text{ nm}} = 80 \text{ M}^{-1} \text{ cm}^{-1}$. Therefore, absorption of the **Fc** $[n]$ CPP photocages extends to the green light, but further red shift to potentially address biological samples with large depth penetration of light would require manipulating the structure of the Cp ligands.

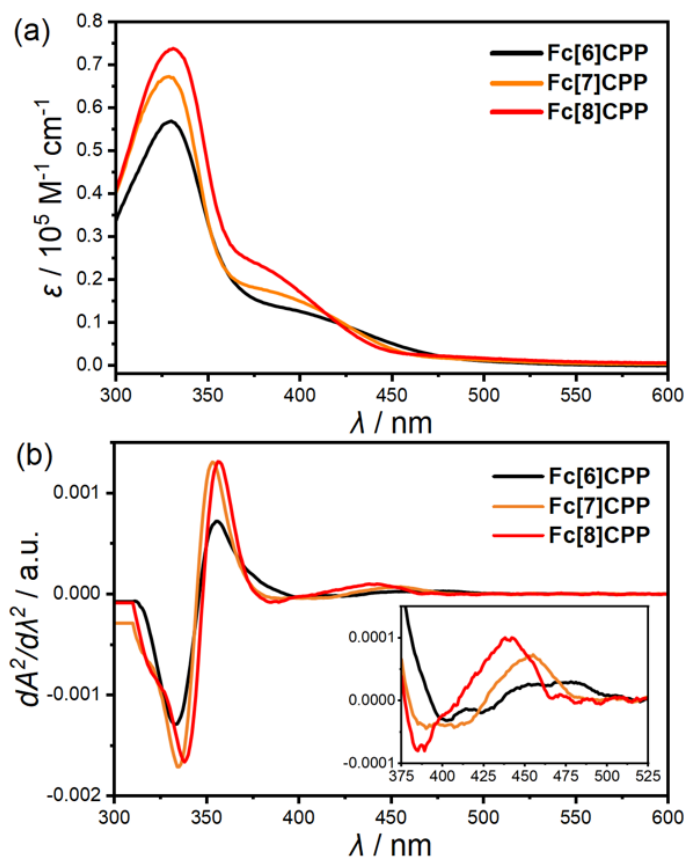


Figure 4.4. (a) UV–vis absorption spectra of **Fc[n]CPPs** ($n = 6–8$) in PhCN. (b) Second derivative of the UV–vis absorption spectra of **Fc[n]CPPs** ($n = 6–8$). The inset highlights the Fc-centered transition.

In our recent report,^[40] we described the ability of **Fc[6]CPP** to undergo a full dissociation of Fe–Cp bond by visible light activation releasing Fe^{2+} , which was analyzed *in situ* by trapping it with 1,10-phenanthroline (phen) forming ferriox complex, $[\text{Fe}(\text{phen})_3]^{2+}$. In analogy to [n]ferrocenophanes, we attributed the remarkable photoreactivity of **Fc[6]CPP** to structural distortion of Fc caused by the high strain of the nano hoop. Here, we tested the photolysis of samples of **Fc[7]CPP** and **Fc[8]CPP** (PhCN, $c \approx 60 \mu\text{M}$) with blue light ($\lambda_{\text{LED}} = 472 \text{ nm}$, 10 mW) and observed the formation of ferriox as a function of time by UV–vis spectroscopy. In the absence of phen, the rate of photolysis of **Fc[8]CPP** appeared slower than that of **Fc[7]CPP** (Figures S4.14–S4.15), while both samples photolyzed slower than **Fc[6]CPP**. The control experiments performed in the dark showed no spectral changes for >24 h at room temperature (Figures S4.16–S4.17). We then tested the ability of **Fc[n]CPPs** ($n = 7–8$) to release the Fe^{2+} ion upon irradiation in the presence of 500 equivalents of phen. After 24 h, all absorption spectra of the filtered

solutions revealed the distinct absorption pattern of $[\text{Fe}(\text{phen})_3]^{2+}$, confirming the photochemical uncaging of Fe^{2+} ions (Figures S4.18–S4.19). It is important to note that the absorption spectrum of independently prepared $[\text{Fe}(\text{phen})_3]^{2+}$ differs subtly from photolyzed solutions due to the presence of precipitates—most probably the released *p*-oligophenylene derivatives. No formation of the $[\text{Fe}(\text{phen})_3]^{2+}$ was observed when the experiment was repeated in the dark (Figures S4.20–S4.21), in contrast to **Fc[6]CPP** for which a low, but noticeable conversion (<10 %) was detected under these conditions.^[40] To quantify the reactivity of **Fc[n]CPPs** ($n = 6-8$), we determined the absolute quantum yields of $[\text{Fe}(\text{phen})_3]^{2+}$ formation in dry, deaerated PhCN for all three compounds (Φ , Table 4.1) under identical conditions ($c = 40 \mu\text{M}$, 500 or 25 equiv. of phen, $\lambda_{\text{LED}} = 472 \text{ nm}$). In the presence of 500 equiv. of phen, we determined the $\Phi = (4.3 \pm 0.3) \times 10^{-2}$ for the most strained **Fc[6]CPP**. The value is slightly lower than that reported Φ previously because we used dry PhCN in this set of experiments to rule out the effects of external perturbations, such as H_2O acting as a nucleophile. Nevertheless, this result reinforces that the presence of water has a positive effect on Fe^{2+} uncaging.^[40] We anticipated that the subtle structural distortion on Fc in the larger nanohoops determined by XRD, electrochemical and spectroscopic analyses would diminish their photochemical reactivity to that of the relatively unstrained pro-aromatic macrocycles, such as **pro-Fc[6]CPP** ($E_{\text{strain}} = 13.7 \text{ kcal mol}^{-1}$),^[40] which shares very similar values of α and δ (1.85° ; 179.1°) with **Fc[n]CPPs** ($n = 7-8$). The quantum yield of $[\text{Fe}(\text{phen})_3]^{2+}$ formation by photolysis of **pro-Fc[6]CPPs** ($\Phi < 5 \times 10^{-5}$) was nearly 1000-fold lower than that of **Fc[6]CPP**. To our surprise, we observed only a slight decrease in the photochemical reactivity for both **Fc[7]CPP** and **Fc[8]CPP** with $\Phi = (2.4 \pm 0.2) \times 10^{-2}$ and $\Phi = (1.3 \pm 0.1) \times 10^{-2}$, respectively. As we reported previously,^[40] the quantum yield with such an excess of phen reaches a value limited by the intersystem crossing quantum yield^[60] of **Fc** and it drops with the decreasing amount of phen, confirming that the Fe–Cp opening is a bimolecular process involving an external ligand. Decreasing the amount of phen to 25 equiv. did not dramatically affect the photolysis of the larger nanohoops either. We observed approximately an order of magnitude difference between the smallest **Fc[6]CPP** and the largest **Fc[8]CPP** with $\Phi = (6.3 \pm 1.4) \times 10^{-3}$ and $\Phi = (7.2 \pm 0.8) \times 10^{-4}$, respectively, supporting the same photochemical mechanism for all compounds in the series. Clearly, the photoreactivity of **Fc[n]CPPs** ($n = 6-8$) must therefore have a different origin than the large strain-induced structural distortion of Fc argued for [n]ferrocenophanes in the literature.

We used DFT calculations of the molecular fragments cropped from the optimized geometries of the ground state **Fc[n]CPPs** ($n = 6-8$) to clarify the observed differences. The Fc fragments from **Fc[n]CPPs** ($n = 7-8$) are relatively unstrained when compared to the fully relaxed **Fc** and the computed strain energy (${}^{\text{Fc}}E_{\text{strain}}$, Table 4.2) is nearly identical to that obtained for Fc in **pro-Fc[6]CPP**. The additional distortion of Fc in **Fc[6]CPP** introduces extra strain energy of only 1.5

kcal mol⁻¹. Clearly, perturbation of Fc to reach values of $\alpha \approx 10^\circ$ and $\delta \approx 173^\circ$ does not impose sufficient strain to enhance the reactivity by more than three orders of magnitude, even if the strain energy was fully projected into the reaction barrier. Further, we compared the calculated ${}^{\text{Fc}}E_{\text{strain}}$ to the known [1]ferrocenophanes. Previously, Müller and co-workers determined the strain energies of [1]ferrocenophanes containing different elements in their bridge by evaluating a homodesmotic reaction (Scheme S4.1) using DFT calculations.^[19] The structure of **Fc[n]CPPs** ($n = 6-8$) prevents us from using the same approach. Therefore, we calculated the strain on the Fc fragments in these [1]ferrocenophanes (Table S4.5) and found a very good correlation (Figure S4.31) with the total strain energies reported by Müller. The lowest strain energy found for a Fc fragment in these [1]ferrocenophanes is >10 kcal mol⁻¹, *i.e.*, significantly more than that determined for **Fc[6]CPP** (${}^{\text{Fc}}E_{\text{strain}} = 2.3$ kcal mol⁻¹), which supports our hypothesis that the enhanced reactivity does not emanate from the Fc perturbation in the nanohoops.

Very recently, Malischewski and co-workers reported synthesis of iron complexes, including ferrocene derivatives, with one highly fluorinated Cp ligand (Cp* = C₅(CF₃)₅).^[45] Such electron-deficient ligand coordinates to Fe²⁺ weakly similar to benzene derivatives. The unstrained FeCpCp* could thus be photolyzed irreversibly in acetonitrile dissociating the Cp* due to markedly weakened Fe–Cp* bond.^[44] In **Fc[n]CPPs** ($n = 6-8$), however, the Cp ligands are strongly coordinating, which is supported by the significantly lower reactivity of the nanohoops in apolar solvents (Figures S4.23–S4.24) that cannot sufficiently stabilize the developing negative charge on the ligand upon Fe–Cp dissociation. Therefore, it must be the strain localized in the curved *para*-phenylenes (${}^{\text{CPP}}E_{\text{strain}}$, Table 4.2) that results in a kinetic rather than thermodynamic effect, *i.e.*, the strain must attenuate the Fe–Cp dissociation barrier at the nucleophilic attack of the external ligand. Such effect would correlate with the observed size-dependent evolution of Φ 's of [Fe(phen)₃]²⁺ formation in **Fc[n]CPPs** ($n = 6-8$). We located the transition states of phen ligand attacking Fc in **Fc[n]CPPs** ($n = 6-8$) and in the parent **Fc** in their lowest triplet states. We note here that DFT calculations of **Fc** and its derivatives in their ground and excited states are notoriously prone to errors.^[61–63] Therefore, the results obtained in this work using a set of various functionals should serve as a qualitative guide to compare the Fe–Cp dissociation in the triplet **Fc[n]CPPs** ($n = 6-8$) and **Fc** assuming that the systematic errors of DFT correlate with the strain in the compounds. Indeed, we observe that the calculated barriers (Table 4.2, see Tables S4.6 and S4.7 for the results from all tested functionals) display the expected trend and correlate markedly better with ${}^{\text{CPP}}E_{\text{strain}}$ than with ${}^{\text{Fc}}E_{\text{strain}}$. The triplet state barrier decreases in the series with increasing the curvature of the hoop-like ligand. We emphasize that the observed effect allows for an elegant strategy to fine-tune the photochemical reactivity of Fc[n]CPPs because majority of the molecular strain is, in fact, distributed in the *para*-phenylenes most distant from Fc. Given the richness of CPP chemistry reported in the past decade, it promises to develop

sophisticated photo- and mechanoactivatable carriers of metal ions beyond iron. In addition, one could argue that the strain energy stored in the curved ligands exerts an internal mechanical force on the Fc unit promoting the Fe–Cp dissociation, which parallels the mechanical stress induced by ultrasound in polymers incorporating **Fc** as a mechanophore. **Fc[n]CPPs (n = 6–8)** could thus be considered as unique (photo)mechanophores and their reactivity suggests that polymers incorporating metallocene mechanophores might be more sensitive to mechanical stress under irradiation.

4.3 Conclusion

In conclusion, we demonstrated a strategy to fine-tune the uncaging efficiency of Fe²⁺ in a series of π -conjugated hoop-like **Fc[n]CPPs (n = 6–8)** that incorporate ferrocene as the iron carrier. As shown by X-ray diffraction and UV–vis analyses, the strain in the macrocycles distorts the structure of Fc moiety and correlates with the nanohoop size. However, this distortion quickly diminishes with the nanohoop size. Yet, even the largest nanohoop with barely perturbed Fc unit displayed a relatively high photochemical uncaging efficiency, in contrast to all previously studied photoactive systems with a structurally distorted ferrocene, such as strained ferrocenophanes. Our results show that the key factor responsible for the unusual Fe–Cp bond dissociation and Fe²⁺ uncaging in Fc[n]CPPs correlates with the intrinsic strain localized in the curved nanohoop ligands, and not with the extent of Fc perturbation. Supported by computational data, we propose that this unexpected effect is kinetic in nature, and it promises controlling the photo- or mechanochemical activation of iron release by precision synthesis known to carbon nanohoops. This study thus expands the current state-of-the-art of photochemistry of ferrocenes, and we believe that it will inspire further advances in the areas of photo- and mechanoresponsive materials that incorporate metallocenes.

4.4 Appendix

All commercially available reagents and chemicals were purchased from Sigma Aldrich, TCI, Fluorochem and Fisher Scientific and used as received without further purification, unless stated otherwise. Anhydrous solvents were purchased from Acros and stored under molecular sieves (4 Å). Technical solvents were bought from VWR International and Biosolve, and were used as received. Unless otherwise stated, all glassware used to perform moisture-sensitive reactions was oven-dried at 120 °C overnight, assembled hot and allowed to cool down to room temperature under a stream of argon, or flame-dried under high vacuum and filled with argon. All reactions that require heating were conducted in an oil bath and the indicated temperature corresponds to the temperature of the oil bath. Flash column chromatography was performed using silica gel 60 Å (230–400 mesh particle size) from Supelco®. Thin layer chromatography (TLC) was performed on silica gel plates F₂₅₄ 60 (aluminum supported) from Supelco® using UV (254 nm) visualization. Recycling gel permeation chromatography (GPC) was performed on LaboAce 5060 preparative HPLC from Japan Analytical Services using chloroform as the solvent. ¹H and ¹³C NMR spectra were recorded on Bruker AV300-II (¹H: 300 MHz, ¹³C: 75 MHz), Bruker AV400 (¹H: 400 MHz, ¹³C: 101 MHz) and Bruker AV500 NEO (¹H: 500 MHz, ¹³C: 126 MHz) spectrometers and analysed using MestReNova software. Chemical shifts (δ) were reported in parts per million (ppm) referenced to residual solvent peak (¹H: 7.26 ppm for CDCl₃, 5.32 ppm for CD₂Cl₂; ¹³C: 77.16 ppm for CDCl₃, 53.84 ppm for CD₂Cl₂). Multiplicities are given as s (singlet), d (doublet), t (triplet), q (quadruplet), m (multiplet), and br (broad). Coupling constants (*J*) are reported in hertz (Hz). High resolution mass spectra (HRMS) were recorded on an AccuTOF LC, JMS-T100LP mass spectrometer (JEOL, Japan). UV–vis spectra were recorded with a double beam spectrophotometer Shimadzu UV2700 equipped with a deuterium lamp (190–350 nm), a halogen lamp (330–900 nm) and a photomultiplier (Hamamatsu R928). Single-crystal X-ray diffraction data measured on a Bruker D8 Quest Eco diffractometer using graphite-monochromated (Triumph) Mo K α radiation (λ = 0.71073 Å) and a CPAD Photon III C14 detector. The sample was cooled with N₂ to 100 K with a Cryostream 700 (Oxford Cryosystems).

4.4.1 Experimental procedures

Compound **1** was prepared according to the reported protocol.^[40]

Preparation of **pro-Fc[7]CPP**

Compound **1** (500 mg, 0.491 mmol, 1 equiv.), 1,4-dibromobenzene (116 mg, 0.491 mmol, 1 equiv., CAS: 106-37-6) and SPhos Pd Gen III (38 mg, 0.049 mmol, 0.1 equiv., CAS: 1445085-82-4) were

introduced in a Schlenk flask. The flask was evacuated and backfilled with nitrogen five times. 1,4-dioxane and 2 M aqueous K_3PO_4 (CAS: 7778-53-2) were sparged with nitrogen for at least 1 hour prior use. 1,4-dioxane (164 mL) was added to the flask and the solution was sparged for 30 minutes, after which it was heated to 80 °C while stirring. After 10 minutes, an aqueous solution of 2 M K_3PO_4 (16.4 mL, 32.7 mmol, 67 equiv.) was added to the flask via cannula. The reaction mixture was stirred at 80 °C for 14 h. After cooling to room temperature, the mixture was filtered through a pad of celite and the reaction flask was rinsed with CH_2Cl_2 . The filtrate was dried over Na_2SO_4 , filtered and concentrated in vacuo. The crude solid was purified by GPC to afford **pro-Fc[7]CPP** as an orange solid (249 mg, 0.296 mmol, 60 %).

Orange solid; $R_f = 0.23$ (SiO_2 , EtOAc: petroleum ether = 1:4).

1H NMR (300 MHz, $CDCl_3$): $\delta = 7.67$ (s, 4H), 7.47 (d, $J = 8.4$ Hz, 4H), 7.31 (d, $J = 8.4$ Hz, 4H), 6.95 (d, $J = 8.4$ Hz, 4H), 6.73 (d, $J = 8.4$ Hz, 4H), 6.48 (d, $J = 10.1$ Hz, 4H), 6.19 (d, $J = 10.1$ Hz, 4H), 4.32 (t, $J = 1.8$ Hz, 4H), 3.80 (t, $J = 1.8$ Hz, 4H), 3.47 (s, 6H), 3.41 (s, 6H).

^{13}C NMR (75 MHz, $CDCl_3$): $\delta = 141.2, 140.0, 139.6, 139.0, 137.9, 134.0, 133.6, 127.8, 127.6, 126.9, 126.4, 125.5, 85.0, 76.1, 75.5, 72.7, 66.1, 52.5, 52.1$.

HRMS (FD+): m/z [M]⁺ calcd for $C_{56}H_{48}O_4Fe$: 840.2903; found: 840.2901.

Preparation of **Fc[7]CPP**

A 0.04 M H_2SnCl_4 solution was prepared by stirring $SnCl_2 \cdot 2H_2O$ (135.3 mg, 0.6 mmol, CAS: 10025-69-1) and concentrated HCl (12 M) (99 μ L, 1.2 mmol, CAS: 7647-01-0) in THF (15 mL) at room temperature for 30 min. After this time, H_2SnCl_4 solution (0.04 M, 10.7 mL, 0.428 mmol, 3.6 equiv.) was added to **pro-Fc[7]CPP** (100 mg, 0.119 mmol, 1 equiv.) and the reaction was stirred at room temperature for 1.5 h. The reaction was quenched with 1 M NaOH (3 mL) and the aqueous layer was extracted with CH_2Cl_2 (3 \times 10 mL). The organic layers were washed with brine, dried over Na_2SO_4 , filtered and concentrated in vacuo to afford **Fc[7]CPP** as orange solid (85 mg, 0.119 mmol, quantitative).

Orange solid; $R_f = 0.40$ (SiO_2 , EtOAc: petroleum ether = 1:4).

1H NMR (300 MHz, CD_2Cl_2): $\delta = 7.56$ (s, 4H), 7.52 (s, 8H), 7.47 (d, $J = 8.4$ Hz, 4H), 7.38 (d, $J = 8.4$ Hz, 4H), 7.27 (d, $J = 8.3$ Hz, 4H), 7.19 (d, $J = 8.3$ Hz, 4H), 4.39 (t, $J = 1.9$ Hz, 4H), 4.28 (t, $J = 1.9$ Hz, 4H).

^{13}C NMR (101 MHz, CD_2Cl_2): $\delta = 140.1, 139.5, 139.0, 138.8, 138.2, 137.7, 137.5, 128.3, 128.1, 128.0, 127.8, 127.6, 88.5, 70.2, 69.1$.

HRMS (FD+): m/z [M]⁺ calcd for $C_{52}H_{36}Fe$: 716.2168; found: 716.2164.

Preparation of **pro-Fc[8]CPP**

Compound **1** (700 mg, 0.687 mmol, 1 equiv.), 4,4'-dibromobiphenyl (214 mg, 0.687 mmol, 1 equiv., CAS: 92-86-4) and SPhos Pd Gen III (54 mg, 0.069 mmol, 0.1 equiv., CAS: 1445085-82-4) were introduced in a Schlenk flask. The flask was evacuated and backfilled with nitrogen five times. 1,4-dioxane and 2 M aqueous K₃PO₄ (CAS: 7778-53-2) were sparged with nitrogen for at least 1 hour prior use. 1,4-dioxane (229 mL) was added to the flask and the solution was sparged for 30 minutes, after which it was heated to 80 °C while stirring. After 10 minutes, an aqueous solution of 2 M K₃PO₄ (22.9 mL, 45.8 mmol, 67 equiv.) was added to the flask via cannula. The reaction mixture was stirred at 80 °C for 14 h. After cooling to room temperature, the mixture was filtered through a pad of celite and the reaction flask was rinsed with CH₂Cl₂. The filtrate was dried over Na₂SO₄, filtered and concentrated in vacuo. The crude solid was purified by GPC to afford **pro-Fc[8]CPP** as an orange solid (244 mg, 0.266 mmol, 39 %).

Orange solid; *R_f* = not measured due to instability on SiO₂.

¹H NMR (300 MHz, CDCl₃): δ = 7.89 (d, *J* = 8.5 Hz, 4H), 7.70 (d, *J* = 8.5 Hz, 4H), 7.52 (d, *J* = 8.6 Hz, 4H), 7.47 (d, *J* = 8.7 Hz, 4H), 7.12 (d, *J* = 8.5 Hz, 4H), 6.94 (d, *J* = 8.4 Hz, 4H), 6.33 (d, *J* = 10.2 Hz, 4H), 6.04 (d, *J* = 10.2 Hz, 4H), 4.48 (t, *J* = 1.8 Hz, 4H), 3.78 (t, *J* = 1.7 Hz, 4H), 3.50 (s, 6H), 3.43 (s, 6H).

¹³C NMR (75 MHz, CDCl₃): δ = 141.9, 140.4, 140.3, 140.0, 138.1, 138.0, 133.9, 133.4, 128.4, 127.6, 127.1, 126.9, 126.2, 125.9, 85.1, 75.4, 75.1, 72.2, 66.9, 52.4, 51.9.

HRMS (FD+): *m/z* [M]⁺ calcd for C₆₂H₅₂O₄Fe: 916.3217; found: 916.3227.

Preparation of **Fc[8]CPP**

A 0.04 M H₂SnCl₄ solution was prepared by stirring SnCl₂·2H₂O (135.3 mg, 0.6 mmol, CAS: 10025-69-1) and concentrated HCl (12 M) (99 μL, 1.2 mmol, CAS: 7647-01-0) in THF (15 mL) at room temperature for 30 min. After this time, H₂SnCl₄ solution (0.04 M, 10.7 mL, 0.428 mmol, 3.6 equiv.) was added to **pro-Fc[8]CPP** (100 mg, 0.109 mmol, 1 equiv.) and the reaction was stirred at room temperature for 1.5 h. The reaction was quenched with 1 M NaOH (3 mL) and the aqueous layer was extracted with CH₂Cl₂ (3 × 10 mL). The organic layers were washed with brine, dried over Na₂SO₄, filtered and concentrated in vacuo to afford **Fc[8]CPP** as orange solid (63.4 mg, 0.080 mmol, 73 %).

Orange solid; *R_f* = not measured due to instability on SiO₂.

¹H NMR (300 MHz, CD₂Cl₂): 7.60 (s, 8H), 7.55 (d, *J* = 8.9 Hz, 4H), 7.50 (d, *J* = 8.9 Hz, 4H), 7.47 (s, 8H), 7.32 (s, 8H), 4.41 (t, *J* = 1.9 Hz, 4H), 4.31 (t, *J* = 1.9 Hz, 4H).

^{13}C NMR (101 MHz, CD_2Cl_2): 140.3, 139.3, 139.2, 138.8, 138.5, 138.3, 138.3, 137.5, 128.3, 128.0, 127.9, 127.9, 127.8, 127.8, 127.6, 127.5, 88.1, 70.1, 69.2.

HRMS (FD+): m/z $[\text{M}]^+$ calcd for $\text{C}_{58}\text{H}_{40}\text{Fe}$: 792.2481; found: 792.2473.

4.4.2 Single crystal X-ray diffraction

X-ray diffraction data of **Fc[7]CPP** and **Fc[8]CPP** were measured on a Bruker D8 Quest Eco diffractometer using graphite-monochromated (Triumph) Mo K α radiation ($\lambda = 0.71073 \text{ \AA}$) and a CPAD Photon III C14 detector. The sample was cooled with N_2 to 100 K with a Cryostream 700 (Oxford Cryosystems). Intensity data were integrated using the SAINT software.^[64] Absorption correction and scaling was executed with SADABS.^[65] The structures were solved using intrinsic phasing with the program SHELXT 2018/2^[66] against F2 of all reflections.

The initial structure solution for **Fc[7]CPP** afforded a $P2_1$ symmetry, however the use of ADDSYM in PLATON^[67] (version 81024) revealed higher symmetry ($P2_1/n$), which was employed in solving the final structure solution.

Least-squares refinement was performed with SHELXL-2019/3.^[68] All non-hydrogen atoms were refined with anisotropic displacement parameters. The hydrogen atoms were introduced at calculated positions with a riding model. CheckCIF revealed no A- or B-level alerts. The X-ray crystallographic data for **Fc[7]CPP** (2464304) and **Fc[8]CPP** (2464305) was deposited at the Cambridge Crystallographic Data Centre (CCDC).

Table S4.1. Crystallographic data and structure refinement details for **Fc[7]CPP** and **Fc[8]CPP**.

Compound	Fc[7]CPP	Fc[8]CPP
CCDC number	2464304	2464305
Empirical formula	$\text{C}_{53}\text{H}_{38}\text{Cl}_2\text{Fe}$	$\text{C}_{64}\text{H}_{52}\text{Fe}$
Formula weight	801.58	876.90
Temperature [K]	100(2)	100(2)
Crystal system	monoclinic	monoclinic
Space group (number)	$P2_1/n$ (14)	$P2_1/n$ (14)
a [Å]	18.3349(8)	20.0159(12)
b [Å]	9.8616(4)	9.8695(6)
c [Å]	21.6582(9)	22.7378(13)
α [°]	90	90
β [°]	97.094(2)	92.150(2)
γ [°]	90	90
Volume [Å³]	3886.1(3)	4488.6(5)
Z	4	4
ρ_{calc} [gcm⁻³]	1.370	1.298
μ [mm⁻¹]	0.564	0.379

F(000)	1664	1848
Crystal size [mm³]	0.238×0.356×0.571	0.141×0.250×0.420
Crystal colour	orange	orange
Crystal shape	block	block
Radiation	MoK α ($\lambda=0.71073$ Å)	MoK α ($\lambda=0.71073$ Å)
2θ range [°]	4.54 to 55.01 (0.77 Å)	4.50 to 55.04 (0.77 Å)
Index ranges	-23 \leq h \leq 23 -12 \leq k \leq 12 -28 \leq l \leq 28	-26 \leq h \leq 25 -12 \leq k \leq 12 -29 \leq l \leq 29
Reflections collected	222895	136117
Independent reflections	8897 $R_{\text{int}} = 0.0452$ $R_{\text{sigma}} = 0.0161$	10309 $R_{\text{int}} = 0.0681$ $R_{\text{sigma}} = 0.0288$
Completeness to $\theta = 25.242^\circ$	99.9 %	99.9 %
Data / Restraints / Parameters	8897 / 538 / 505	10309 / 618 / 586
Absorption correction T_{min}/T_{max} (method)	0.6105 / 0.7456 (multi-scan)	0.6795 / 0.7456 (multi-scan)
Goodness-of-fit on F^2	1.146	1.037
Final R indexes [$\geq 2\sigma(I)$]	$R_1 = 0.0848$ $wR_2 = 0.2233$	$R_1 = 0.0606$ $wR_2 = 0.1695$
Final R indexes [all data]	$R_1 = 0.0868$ $wR_2 = 0.2244$	$R_1 = 0.0684$ $wR_2 = 0.1776$
Largest peak/hole [eÅ⁻³]	0.55/-0.65	1.69/-0.76

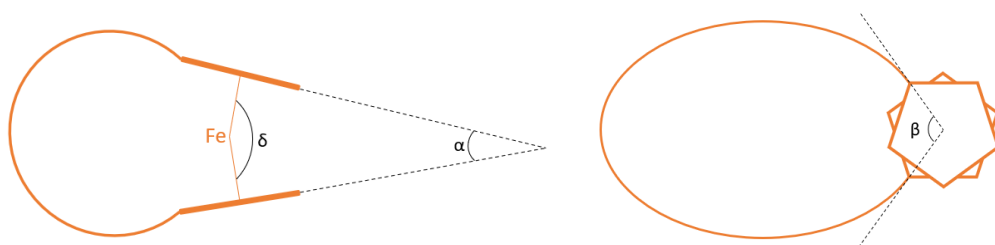


Figure S4.1. Definition of angles α , δ and β used to characterize structural features of ferrocenophanes.

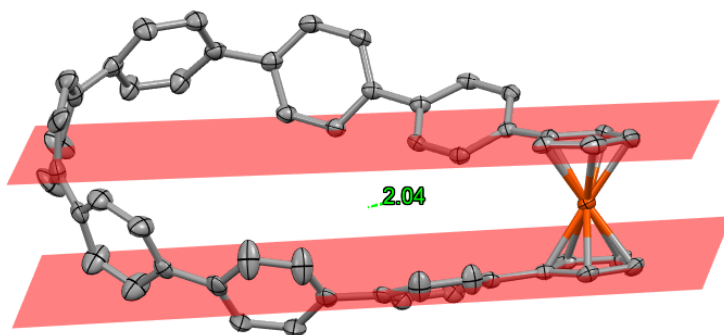


Figure S4.2. Tilt angle α between Cp rings in **Fc[7]CPP** (ellipsoids shown at 50% probability; all hydrogen atoms and solvent were omitted for clarity).

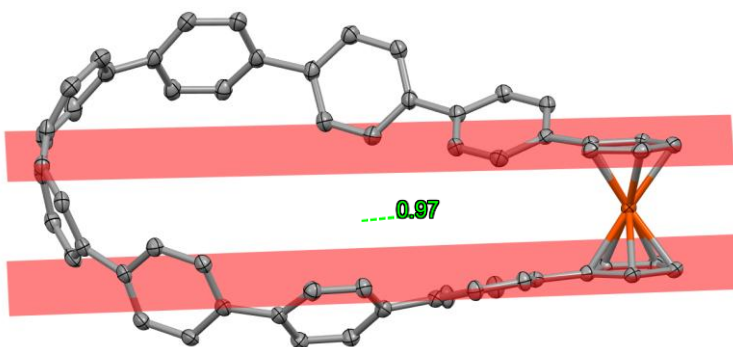


Figure S4.3. Tilt angle α between Cp rings in **Fc[8]CPP** (thermal ellipsoids shown at 50% probability; all hydrogen atoms and solvent were omitted for clarity).

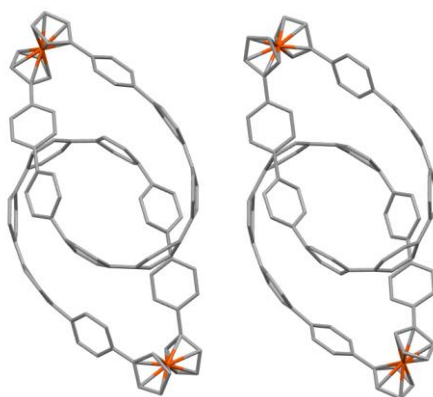


Figure S4.4. Packing of **Fc[7]CPP** (all hydrogen atoms and solvent were omitted for clarity).

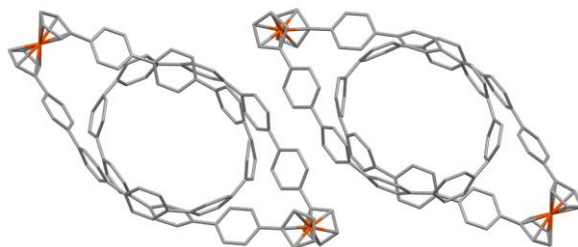


Figure S4.5. Packing of **Fc[8]CPP** (all hydrogen atoms and solvent were omitted for clarity).

4.4.3 Electrochemical measurements

Cyclic voltammetry (CV) and differential pulse voltammetry (DPV) experiments were conducted using a Metrohm Autolab potentiostat running Nova 1.11 software. A glassy carbon working electrode (diameter of electrode disk 2 mm \pm 0.1 mm), a platinum counter electrode and a leakless Ag/AgCl reference electrode were used. Measurements of 1,1,2,2-tetrachloroethane solutions of a sample (1 mM) were conducted at room temperature under a N₂ atmosphere in the dark in the presence of a supporting electrolyte (*n*-Bu₄NPF₆, 0.1 M). Dried and degassed (3 \times freeze-pump-thaw cycle) 1,1,2,2-tetrachloroethane was used. Supporting electrolyte *n*-Bu₄NPF₆ was recrystallized from ethanol three times. The measurements were conducted in the presence of decamethylferrocene (DmFc) used as reference. The potentials were calibrated with respect to the decamethylferrocene/decamethylferrocenium couple (Me₁₀Fc/Me₁₀Fc⁺) at -0.561 V vs Ag/AgCl (= with respect to the ferrocene/ferrocenium couple (Fc/Fc⁺) at 0.00 V vs Ag/AgCl).

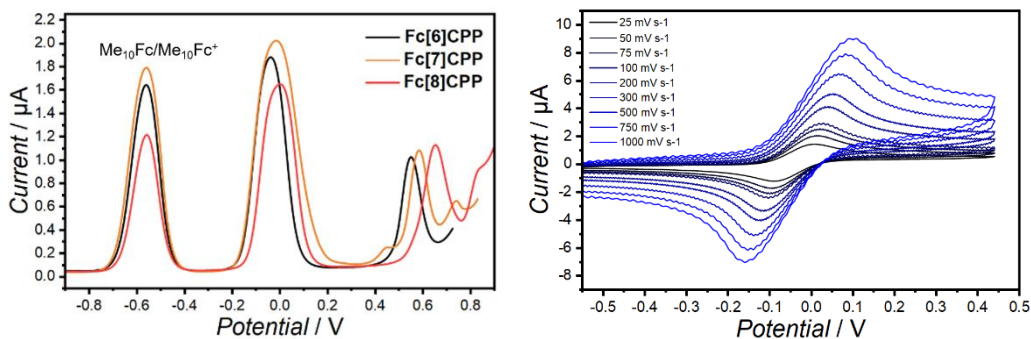


Figure S4.6 (left). Differential pulse voltammetry (DPV) (scan rate = 10 mV s⁻¹) of **Fc[*n*]CPPs** (*n* = 6–8) and decamethylferrocene (Me₁₀Fc) used as internal standard recorded in 0.1 M *n*-Bu₄NPF₆/1,1,2,2-tetrachloroethane. Data referenced vs **Fc/Fc⁺**.

Figure S4.7 (right). Cyclic voltammetry (first oxidation) of **Fc[6]CPP** recorded in 0.1 M *n*-Bu₄NPF₆/1,1,2,2-tetrachloroethane at different scan rates and referenced against **Fc/Fc⁺**.

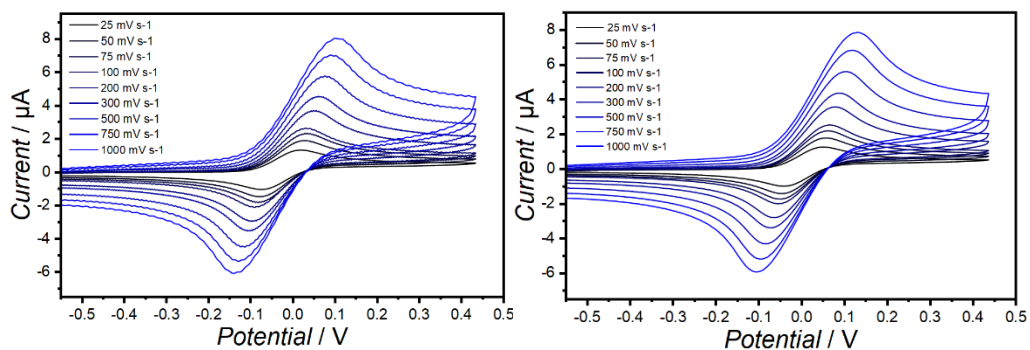


Figure S4.8 (left). Cyclic voltammetry (first oxidation) of **Fc[7]CPP** recorded in 0.1 M *n*-Bu₄NPF₆/1,1,2,2-tetrachloroethane at different scan rates and referenced against **Fc/Fc⁺**.

Figure S4.9 (right). Cyclic voltammetry (first oxidation) of **Fc[8]CPP** recorded in 0.1 M *n*-Bu₄NPF₆/1,1,2,2-tetrachloroethane at different scan rates and referenced against **Fc/Fc⁺**.

Table S4.2. $E_{1/2}$ values of **Fc[n]CPPs** ($n = 6-8$) in 0.1 M *n*-Bu₄NPF₆/1,1,2,2-tetrachloroethane obtained by CV and DPV and referenced against **Fc/Fc⁺** (three independent measurements for each compound).

Compd.	Meas. ^a	$E_{1/2}$ (1 st	$E_{1/2}$ (1 st	$E_{1/2}$ (2 nd	$E_{1/2}$ (2 nd
		oxidation) vs Fc/Fc ⁺ (V) (from CV at $\nu = 100$ mV s ⁻¹)	oxidation) vs Fc/Fc ⁺ (V) (from DPV at $\nu = 100$ mV s ⁻¹)	oxidation ^b) vs Fc/Fc ⁺ (V) (from CV at $\nu = 100$ mV s ⁻¹)	oxidation) vs Fc/Fc ⁺ (V) (from DPV at $\nu = 100$ mV s ⁻¹)
Fc[6]CPP	1	-0.030	-0.055	0.648	0.577
	2	-0.036	-0.027	0.622	0.584
	3	-0.028	-0.041	0.626	0.570
	Average ± STD^c	-0.031 ± 0.003	-0.041 ± 0.011	0.632 ± 0.011	0.577 ± 0.006
Fc[7]CPP	1	-0.014	-0.012	0.660	0.588
	2	-0.027	0.001	0.668	0.619
	3	-0.006	-0.013	0.683	0.591
	Average ± STD^c	-0.016 ± 0.009	-0.008 ± 0.006	0.670 ± 0.010	0.599 ± 0.014
Fc[8]CPP	1	0.014	0.015	0.759	0.675
	2	0.008	0.001	0.746	0.668
	3	0.031	-0.013	0.753	0.682
	Average ± STD^c	0.018 ± 0.010	0.001 ± 0.011	0.753 ± 0.005	0.675 ± 0.006

^a Meas. = measurement number. ^b Measured at the anodic peak. ^c STD = standard deviation of the mean.

The reversibility was assessed by plotting the square root of the scan rate (ν) against the anodic peak current ($i_{p,a}$) from CV (Randles–Ševčík equation).

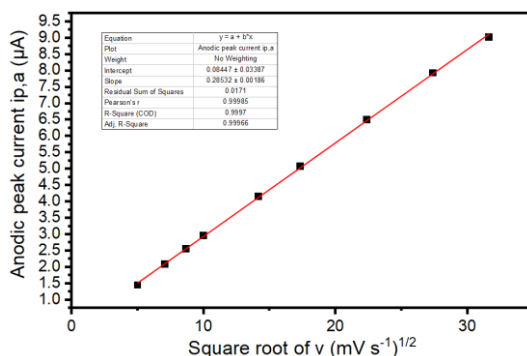


Figure S4.10. Square root of the scan rate (ν) against the anodic peak current ($i_{p,a}$) showing the reversibility of the first oxidation of **Fc[6]CPP**.

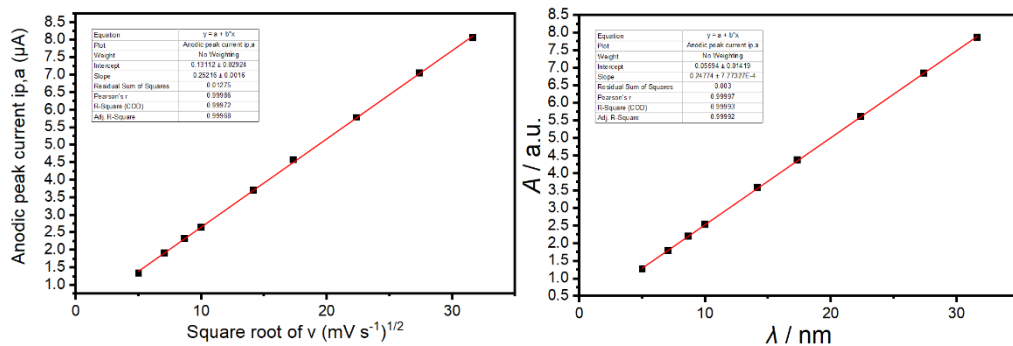


Figure S4.11 (left). Square root of the scan rate (v) against the anodic peak current ($i_{p,a}$) showing the reversibility of the first oxidation of **Fc[7]CPP**.

Figure S4.12 (right). Square root of the scan rate (v) against the anodic peak current ($i_{p,a}$) showing the reversibility of the first oxidation of **Fc[8]CPP**.

4.4.4 Photophysical studies

4.4.4.1 Derivative absorption spectra

The first and second derivative absorption spectra of **Fc[n]CPPs** ($n = 6-8$) were obtained from absorption spectra measured in PhCN in Origin using Savitzky-Golay smooth.

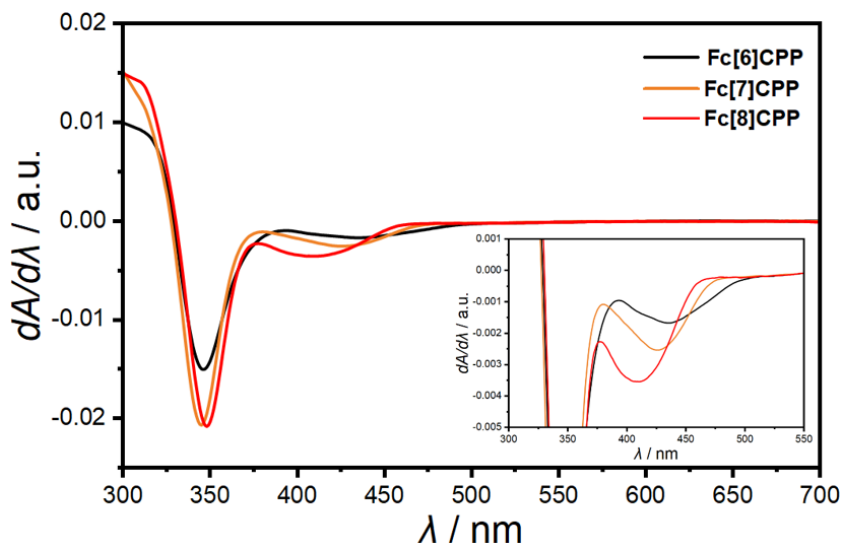


Figure S4.13. First derivative of the absorption spectra of **Fc[n]CPPs** ($n = 6-8$) in PhCN.

4.4.4.2 Determination of absorption coefficients

The average absorption coefficient ϵ of each compound in benzonitrile (PhCN) was determined by three series of dilutions from three independent stock solutions.

Table S4.3. Absorption coefficients ϵ of **Fc[n]CPPs** ($n = 6-8$) in PhCN at different wavelengths.

Compd.	Meas. ^a	ϵ_{\max}^b ($M^{-1} \text{ cm}^{-1}$)	ϵ_{472} ($M^{-1} \text{ cm}^{-1}$)	ϵ_{525} ($M^{-1} \text{ cm}^{-1}$)
Fc[6]CPP	1	52493	2421	727
	2	59491	2682	687
	3	58882	2603	655
	Average \pm STD^c	56956 \pm 3165	2569 \pm 109	690 \pm 29
Fc[7]CPP	1	64737	1512	401
	2	67272	1563	405
	3	69974	1620	408
	Average \pm STD^c	67328 \pm 2138	1565 \pm 44	405 \pm 3
Fc[8]CPP	1	74877	1420	391
	2	73352	1403	388
	3	73384	1430	401
	Average \pm STD^c	73871 \pm 712	1418 \pm 13	393 \pm 6

^a Meas. = measurement number. ^b Measured at 330 nm for **Fc[6]CPP**, 329 nm for **Fc[7]CPP** and 331 nm for **Fc[8]CPP**. ^c STD = standard deviation of the mean.

4.4.4.3 Photoreactivity studies

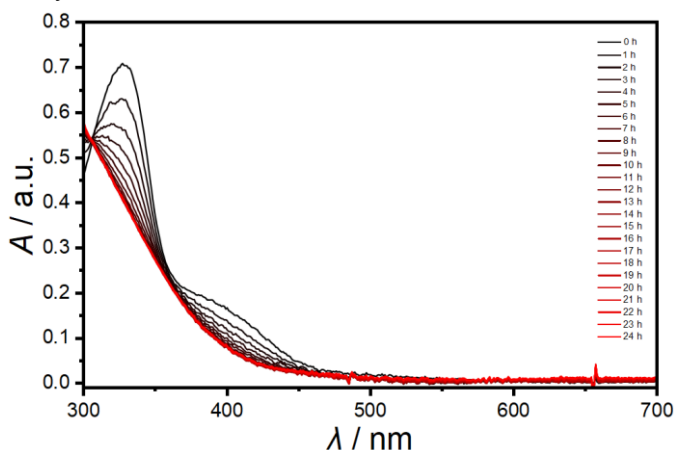


Figure S4.14. Absorption spectra of **Fc[7]CPP** in PhCN ($\approx 10 \mu\text{M}$) irradiated with blue light (472 nm, 10 mW) and stirred at room temperature.

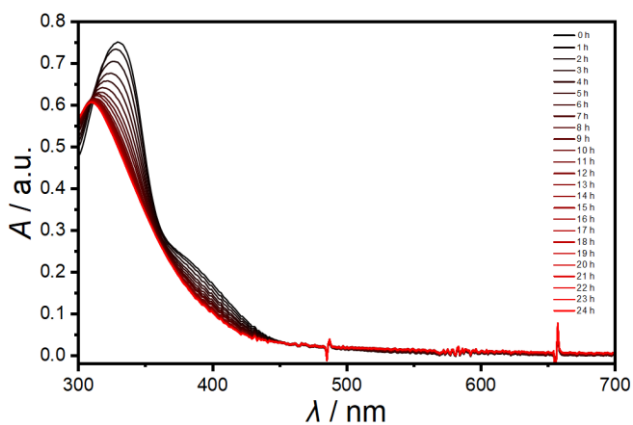


Figure S4.15. Absorption spectra of Fc[8]CPP in PhCN ($\approx 10 \mu\text{M}$) irradiated with blue light (472 nm, 10 mW) and stirred at room temperature.

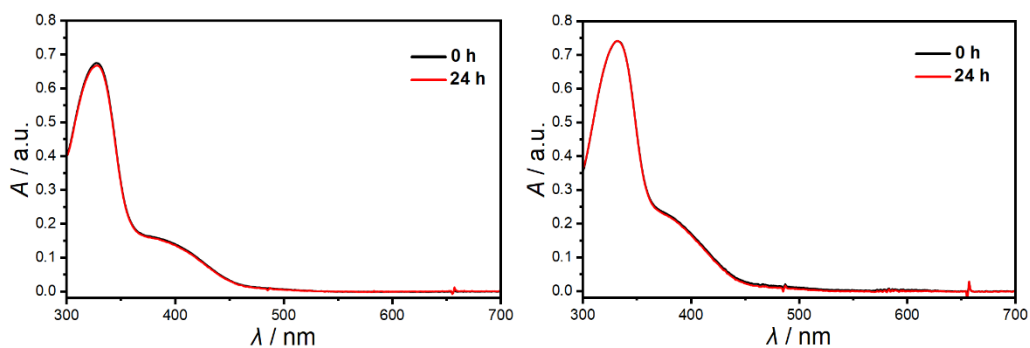


Figure S4.16 (left). Absorption spectra of Fc[7]CPP in PhCN ($\approx 10 \mu\text{M}$) stirred in the dark at room temperature.

Figure S4.17 (right). Absorption spectra of Fc[8]CPP in PhCN ($\approx 10 \mu\text{M}$) stirred in the dark at room temperature.

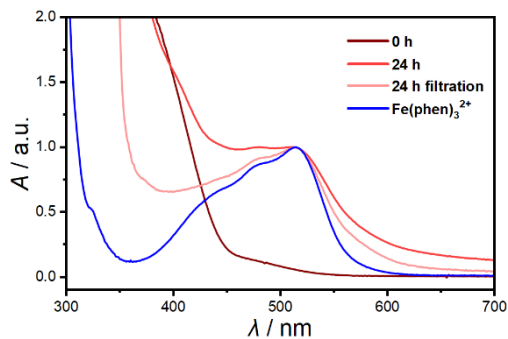
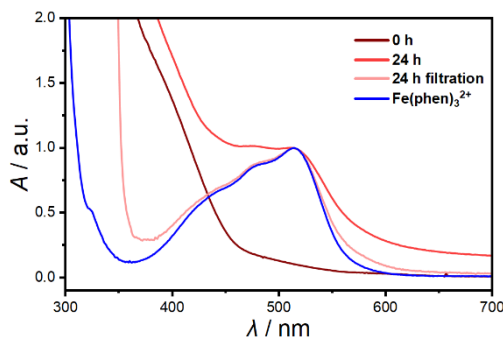


Figure S4.18 (left). Normalized absorption spectra of **Fc[7]CPP** in PhCN ($\approx 60 \mu\text{M}$, phen: 500 equiv.) irradiated with blue light (472 nm, 10 mW) and stirred at room temperature for 24 h (red: unfiltered, light red: filtered) and independently prepared $[\text{Fe}(\text{phen})_3]^{2+}$ (blue). The spectrum at 0 h (dark red) was scaled to match the ϵ of $[\text{Fe}(\text{phen})_3]^{2+}$.

Figure S4.19 (right). Normalized absorption spectra of **Fc[8]CPP** in PhCN ($\approx 60 \mu\text{M}$, phen: 500 equiv.) irradiated with blue light (472 nm, 10 mW) and stirred at room temperature for 24 h (red: unfiltered, light red: filtered) and independently prepared $[\text{Fe}(\text{phen})_3]^{2+}$ (blue). The spectrum at 0 h (dark red) was scaled to match the ϵ of $[\text{Fe}(\text{phen})_3]^{2+}$.

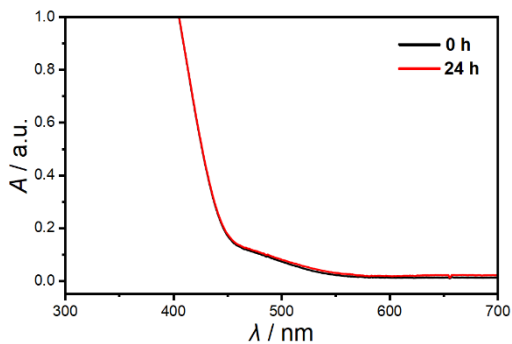
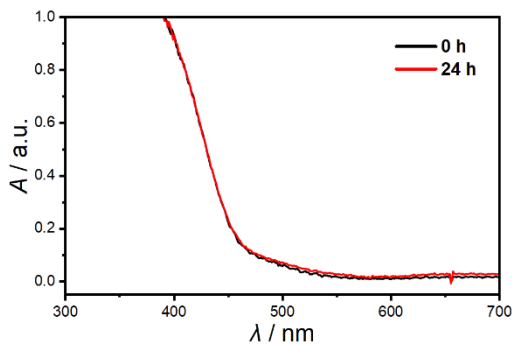


Figure S4.20 (left). Absorption spectra of **Fc[7]CPP** in PhCN ($\approx 60 \mu\text{M}$) + phen (500 equiv.) stirred in the dark at room temperature.

Figure S4.21 (right). Absorption spectra of **Fc[8]CPP** in PhCN ($\approx 60 \mu\text{M}$) + phen (500 equiv.) stirred in the dark at room temperature.

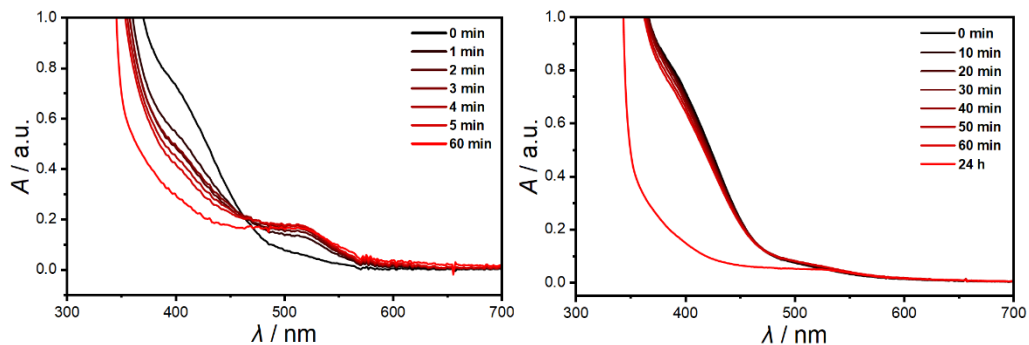


Figure S4.22 (left). Absorption spectra of Fc[6]CPP in PhCN (≈ 60 μM) + phen (250 equiv) irradiated with blue light (472 nm, 10 mW) and stirred at room temperature.

Figure S4.23 (right). Absorption spectra of Fc[6]CPP in toluene (≈ 60 μM) + phen (250 equiv) irradiated with blue light (472 nm, 10 mW) and stirred at room temperature.

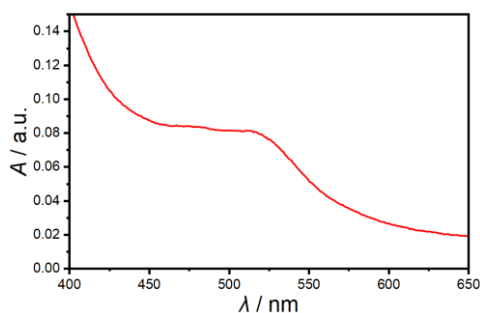


Figure S4.24. Absorption spectrum of the precipitate, from the irradiation of Fc[6]CPP in toluene (≈ 60 μM) + phen (250 equiv) with blue light (472 nm, 10 mW) over 24 h, dissolved in PhCN and showing the band of the [Fe(phen)₃]²⁺ complex.

4.4.4.4 Quantum yields of $[Fe(phen)_3]^{2+}$ complex formation

For details concerning the theory of quantum yield calculation, see Appendix 3.4.4.5.

General procedure for sample preparation: to a 40 μ M solution of **Fc[n]CPP** in PhCN was added 25 equiv. or 500 equiv. of 1,10-phenanthroline (= phen):

- 25 equiv.: 100 μ L of 0.0296 M phen stock solution
- 500 equiv.: 120 μ L of 0.5 M phen stock solution

The sample (total volume = 3.00 mL) was prepared in a quartz cuvette covered in aluminum foil and degassed by bubbling N_2 for 20 min. It was then irradiated (472 nm, $\Phi_e = 2.40$ –9.05 mW) for 2–5 min while stirring. The experiment was repeated four times. PhCN was distilled under vacuum and dried over Al_2O_3 prior to use.

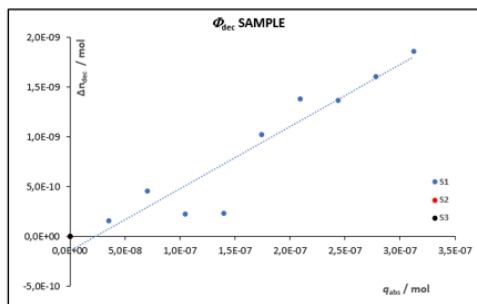
Table S4.4. Quantum yields of $[Fe(phen)_3]^{2+}$ complex formation from **Fc[n]CPPs** ($n = 6$ –8) in PhCN in the presence of phen upon irradiation with a 472 nm light source.

Compd.	phen (equiv.)	Φ_e (mW)	Φ_{form}	Average	STD ^a
Fc[6]CPP	25	9.05	0.00623	$6.25 \cdot 10^{-3}$	$1.40 \cdot 10^{-3}$
			0.00436		
			0.00608		
			0.00831		
Fc[7]CPP	25	9.05	0.00183	$1.96 \cdot 10^{-3}$	$4.46 \cdot 10^{-4}$
			0.00182		
			0.00150		
			0.00270		
Fc[8]CPP	25	9.05	0.000615	$7.18 \cdot 10^{-4}$	$7.84 \cdot 10^{-5}$
			0.000799		
			0.000669		
			0.000789		
Fc[6]CPP	500	2.40	0.0391	$4.30 \cdot 10^{-2}$	$3.21 \cdot 10^{-3}$
			0.0437		
			0.0478		
			0.0414		
Fc[7]CPP	500	2.40	0.0198	$2.37 \cdot 10^{-2}$	$2.25 \cdot 10^{-3}$
			0.0255		
			0.0248		
			0.0245		
Fc[8]CPP	500	2.40	0.0126	$1.26 \cdot 10^{-2}$	$7.89 \cdot 10^{-4}$
			0.0139		
			0.0118		
			0.0122		

^a STD = standard deviation of the mean.

Representative examples of the obtained slopes (= quantum yields):

$$\Phi_{\text{form}} = 6,23\text{E-}03 \pm 0,0\text{E+}00$$



$$\Phi_{\text{form}} = 1,82\text{E-}03 \pm 0,0\text{E+}00$$

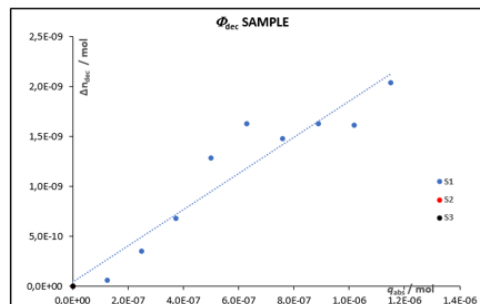
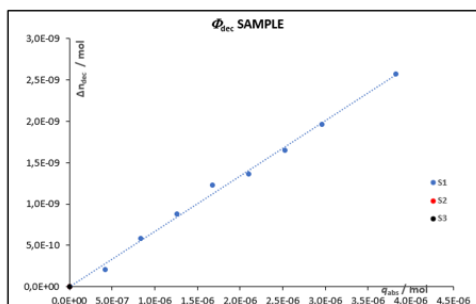


Figure S4.25 (left). Fc[6]CPP + phen (25 equiv.). Note that the error is not reported because a single dataset is displayed.

Figure S4.26 (right). Fc[7]CPP + phen (25 equiv.). Note that the error is not reported because a single dataset is displayed.

$$\Phi_{\text{form}} = 6,69\text{E-}04 \pm 0,0\text{E+}00$$



$$\Phi_{\text{form}} = 4,37\text{E-}02 \pm 0,0\text{E+}00$$

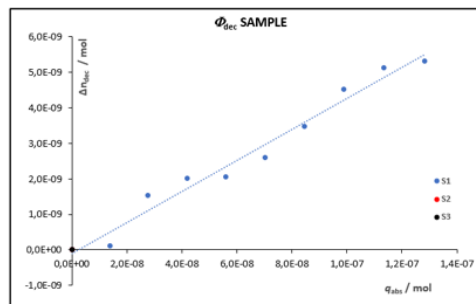
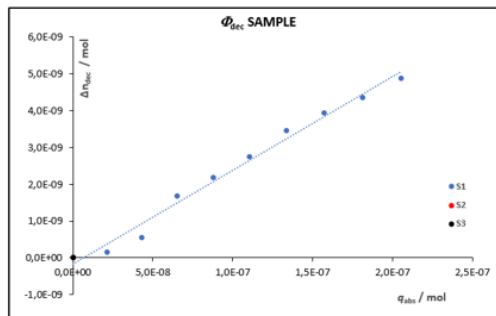


Figure S4.27 (left). Fc[8]CPP + phen (25 equiv.). Note that the error is not reported because a single dataset is displayed.

Figure S4.28 (right). Fc[6]CPP + phen (500 equiv.). Note that the error is not reported because a single dataset is displayed.

$$\Phi_{\text{form}} = 2,55\text{E-}02 \pm 0,0\text{E+}00$$



$$\Phi_{\text{form}} = 1,26\text{E-}02 \pm 0,0\text{E+}00$$

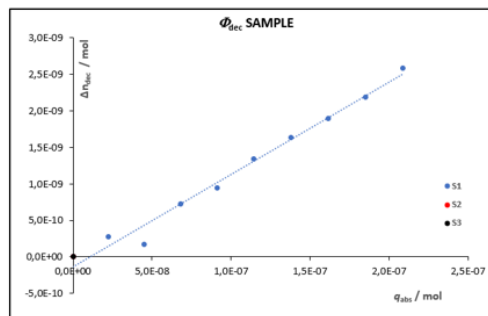
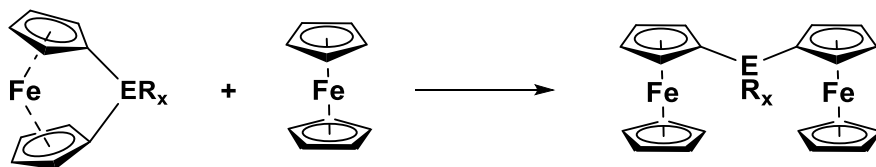


Figure S4.29 (left). Fc[7]CPP + phen (500 equiv.). Note that the error is not reported because a single dataset is displayed.

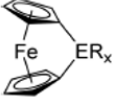
Figure S4.30 (right). Fc[8]CPP + phen (500 equiv.). Note that the error is not reported because a single dataset is displayed.

4.4.5 DFT calculations



Scheme S4.1. Homodesmotic reaction used by Müller and co-workers^[19] to determine the strain energies of [1]ferrocenophanes (ER_x = bridging group).

Table S4.5. Comparison of the calculated^a FcE_{strain} localized on the Fc fragment cropped from the structure of the corresponding [1]ferrocenophanes and the isodesmic reaction approach of Müller and co-workers.^[19]

	FcE_{strain} (kcal mol ⁻¹)		Müller (kcal mol ⁻¹)
	D3B3LYP	wB97XD	
SiMe ₂	-10.2	-10.6	-18.3
BN(SiMe ₃) ₂	-24.2	-24.5	-25.6
CMe ₂	-33.6	-33.8	-29.8
PMe	-16.4	-16.6	-23.3

^a Values calculated on Fc fragments from [1]ferrocenophanes optimized at the B3LYP/6-31G(d) level of theory. The fragments were obtained by removing the corresponding [1]ferrocenophane bridge and filling the valency on the bridging carbon atoms in the Cp's with two hydrogen atoms. The coordinates of the added hydrogen atoms were then fully relaxed while all other coordinates of the remaining atoms in the Fc fragment kept frozen.

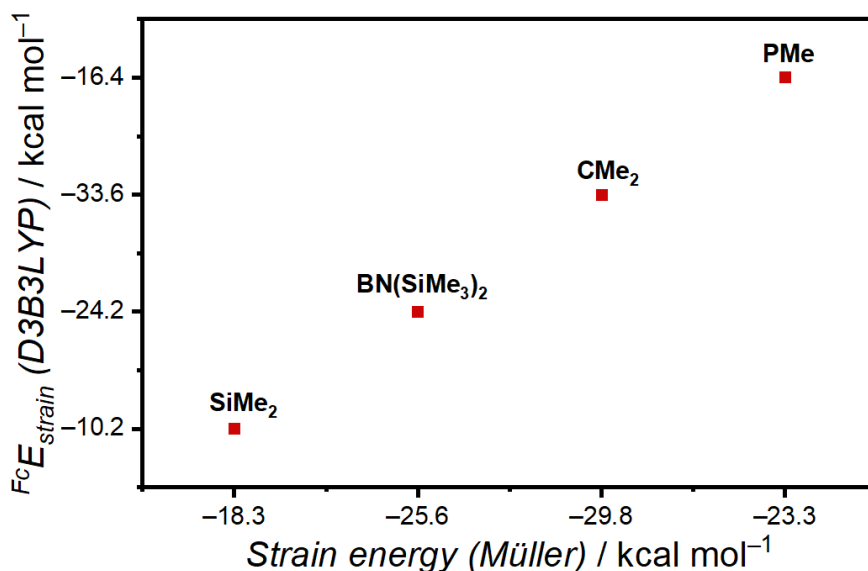


Figure S4.31. Graph showing the correlation between the calculated (D3B3LYP) FcE_{strain} localized on the Fc fragment cropped from the structure of [1]ferrocenophanes and the strain energies of the corresponding [1]ferrocenophanes reported by Müller and co-workers.^[19]

Table S4.6. The calculated^a transition state energies (ΔH^\ddagger) of the nucleophilic attack of phen on the Fc unit in triplet **Fc**[*n*]**CPPs** (*n* = 6–8) and **Fc** on the BP86/6-31G(d) optimized geometries.

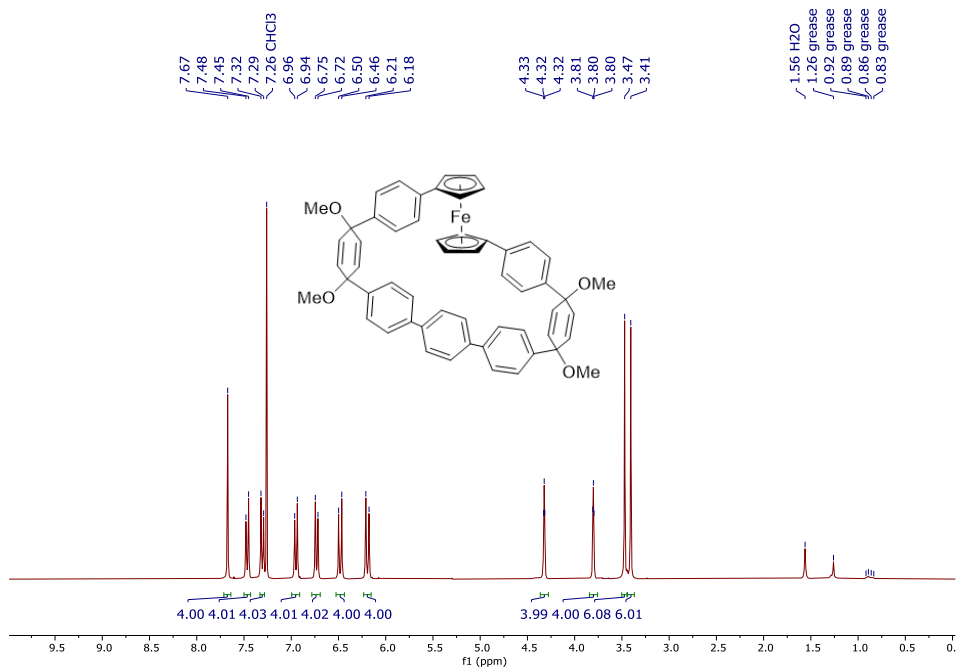
Compd.	$\Delta H^\ddagger / \text{kcal mol}^{-1}$							
	D3B3LYP	wB97XD	D3BLYP	B97D	M06L	M06-2X	MN15	PBE0
Fc [6] CPP	-1.1	4.8	-4.7	-5.7	-0.6	-2.4	6.6	1.6
Fc [7] CPP	-0.4	4.6	-4.3	-5.5	-0.1	-2.1	6.8	2.2
Fc [8] CPP	2.3	7.3	-1.9	-3.6	1.2	0.7	9.3	4.8
Fc	6.8	10.5	2.8	1.8	7.2	2.5	11.3	10.1

^a Values (0K) calculated with the corresponding functional and cc-pVTZ basis set on the BP86/6-31G(d) optimized geometries including the unscaled ZPVE correction and empirical dispersion correction (D3).

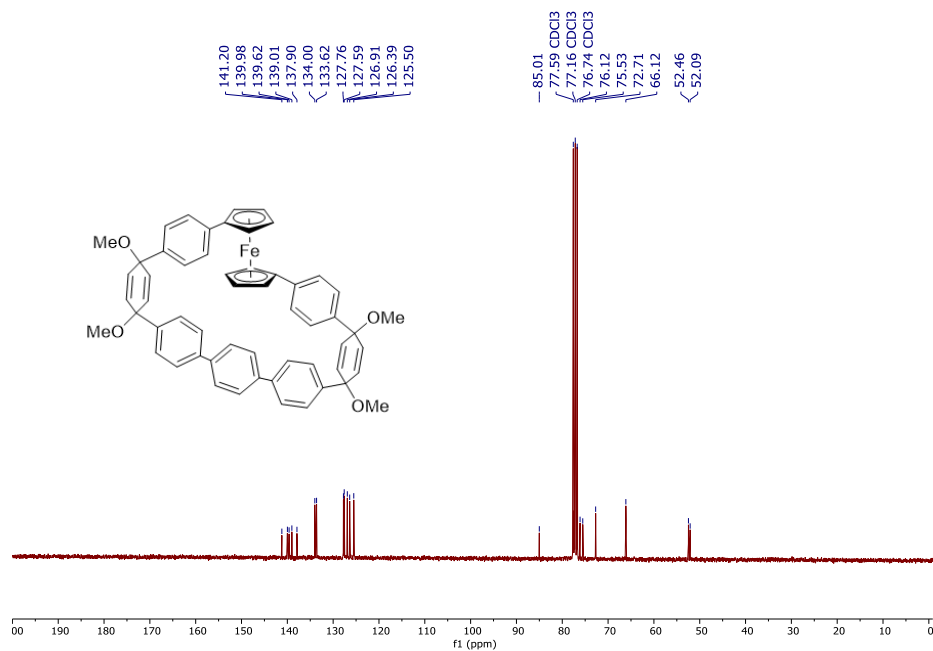
Table S4.7. The calculated^a transition state energies (ΔH^\ddagger) of the nucleophilic attack of phen on the Fc unit in triplet **Fc**[*n*]**CPPs** (*n* = 6–8) and **Fc** on the B3LYP/6-31G(d) optimized geometries.

Compd.	$\Delta H^\ddagger / \text{kcal mol}^{-1}$							
	D3B3LYP	wB97XD	D3BLYP	B97D	M06L	M06-2X	MN15	PBE0
Fc [6] CPP	-3.0	3.0	-4.5	-5.1	0.8	-4.5	12.0	0.3
Fc [7] CPP	-2.5	2.8	-4.1	-4.8	1.6	-4.4	12.3	0.8
Fc [8] CPP	0.2	5.5	-1.4	-2.3	3.2	-1.5	14.8	3.5
Fc	4.5	8.3	3.7	2.9	8.9	-2.8	11.1	6.8

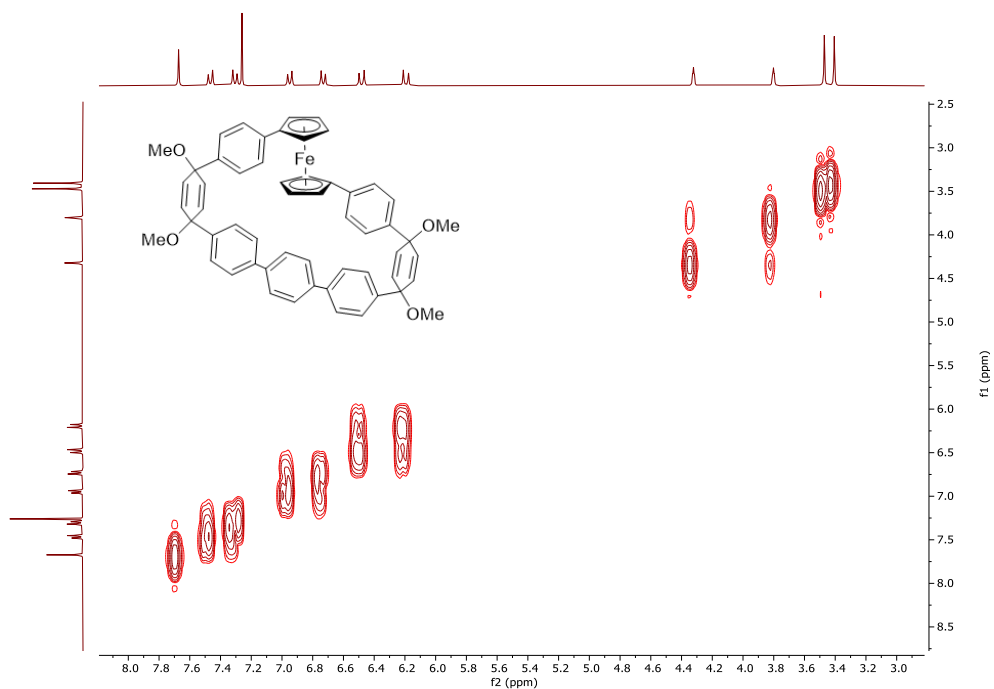
^a Values (0K) calculated with the corresponding functional and cc-pVTZ basis set on the B3LYP/6-31G(d) optimized geometries including the unscaled ZPVE correction and empirical dispersion correction (D3).

4.4.6 ^1H and ^{13}C NMR spectra

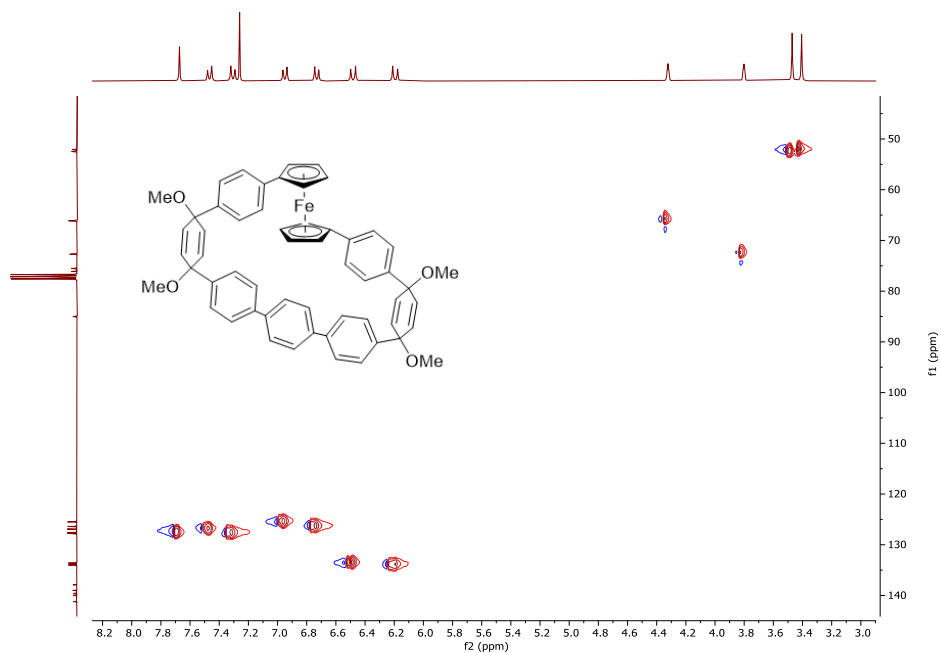
^1H NMR spectrum of **pro-Fc[7]CPP** in CDCl_3 (300 MHz).



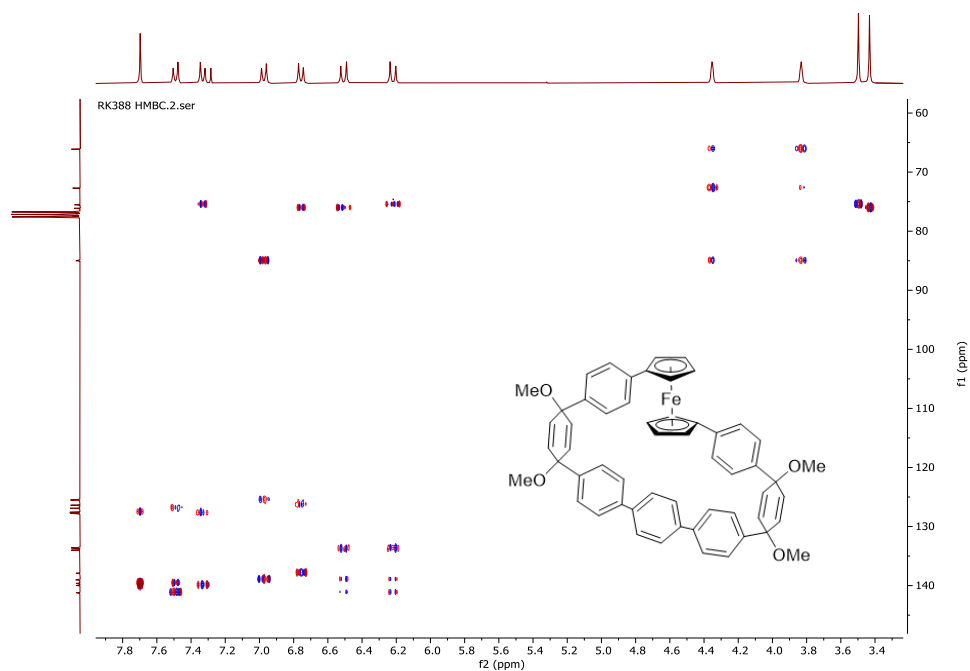
^{13}C NMR spectrum of **pro-Fc[7]CPP** in CDCl_3 (75 MHz).



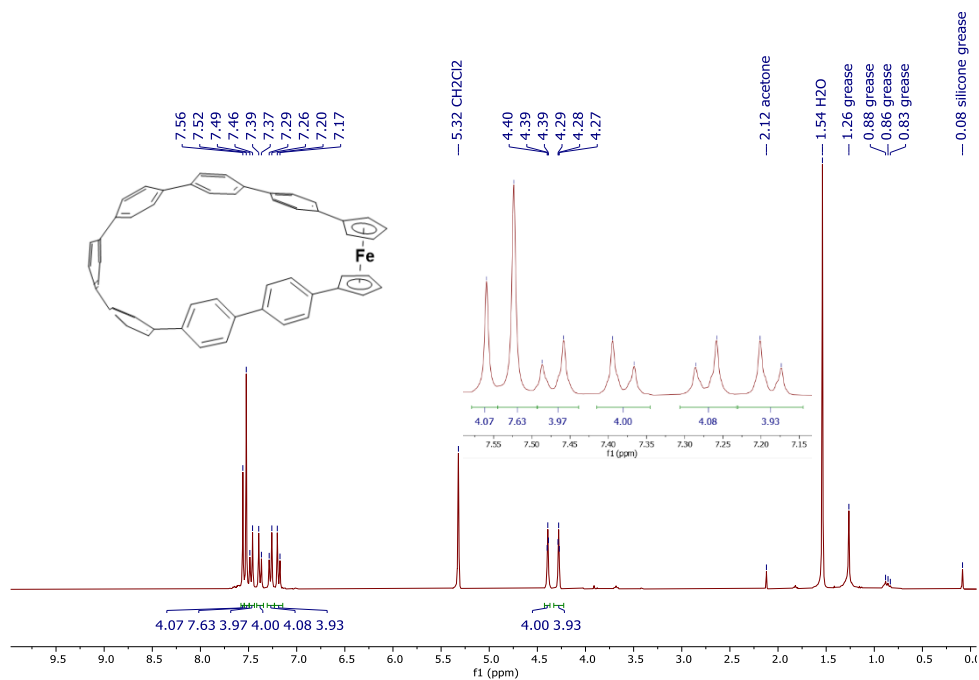
^1H - ^1H COSY spectrum of compound **pro-Fc[7]CPP** in CDCl_3 (300 MHz).



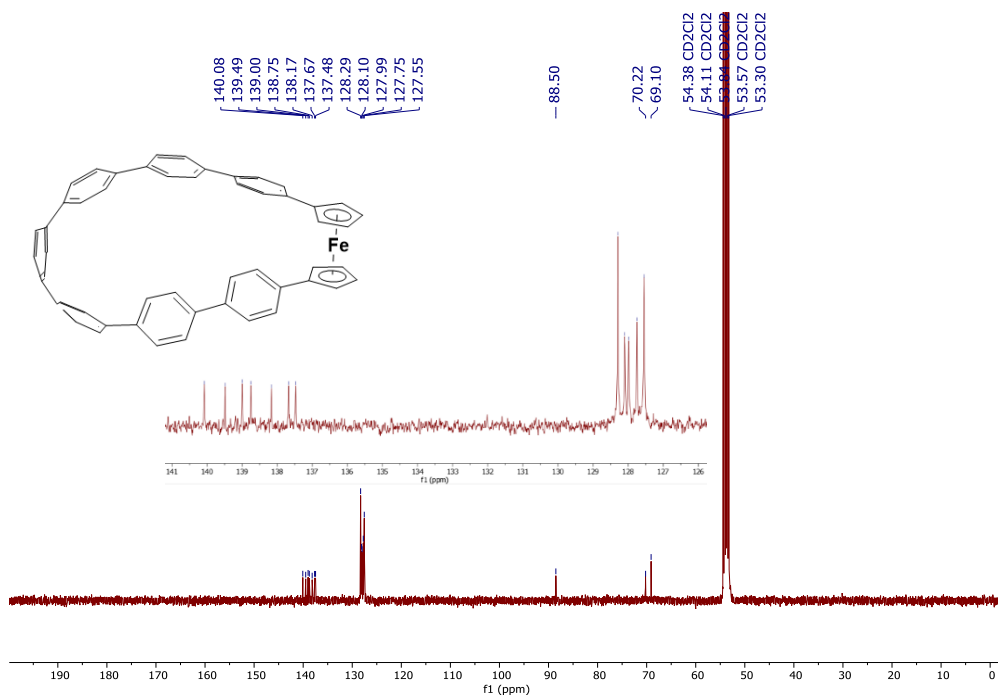
^1H - ^{13}C HSQC spectrum of compound **pro-Fc[7]CPP** in CDCl_3 (300/75 MHz).



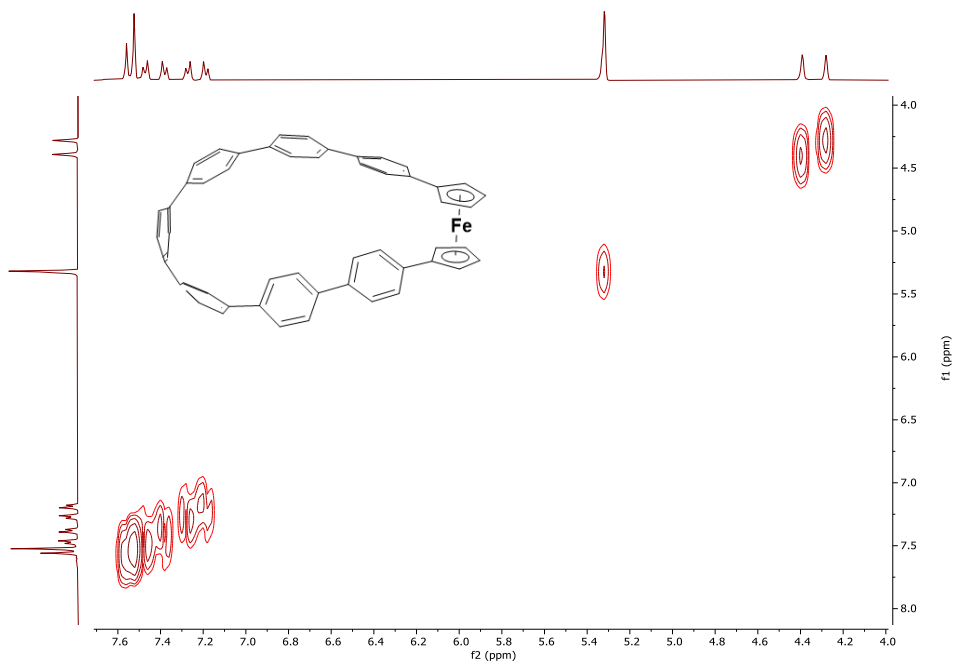
^1H - ^{13}C HMBC spectrum of compound **pro-Fc[7]CPP** in CDCl_3 (300/75 MHz).



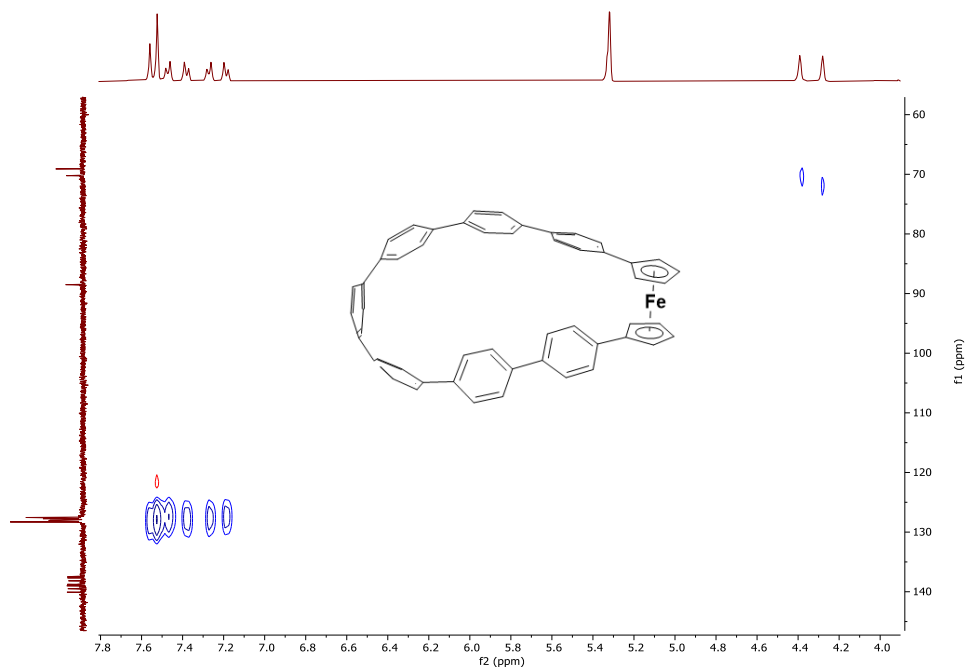
^1H NMR spectrum of compound **Fc[7]CPP** in CD_2Cl_2 (300 MHz).



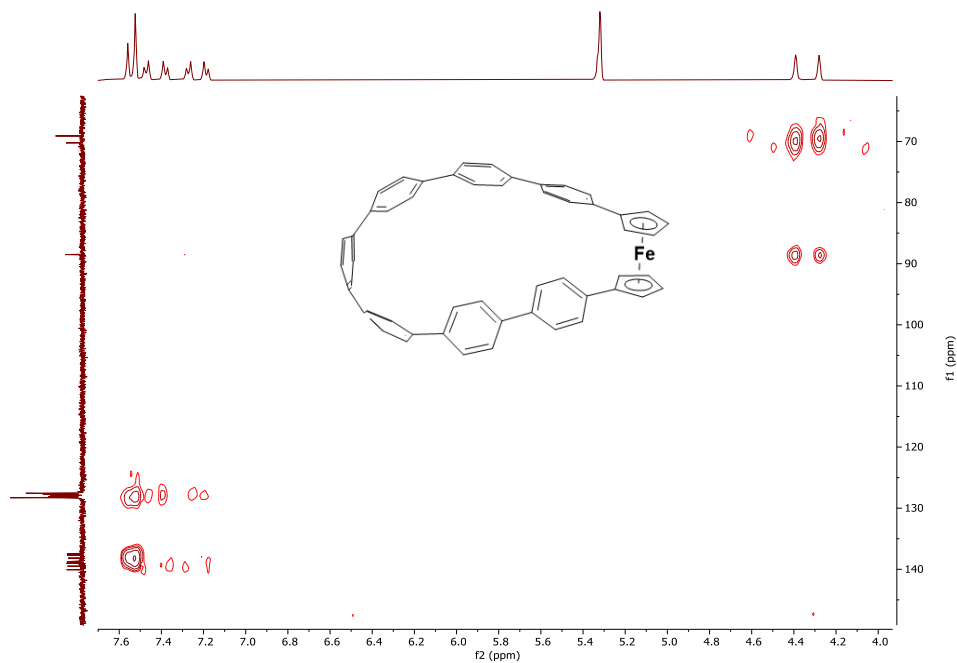
¹³C NMR spectrum of compound **Fc[7]CPP** in CD₂Cl₂ (101 MHz).



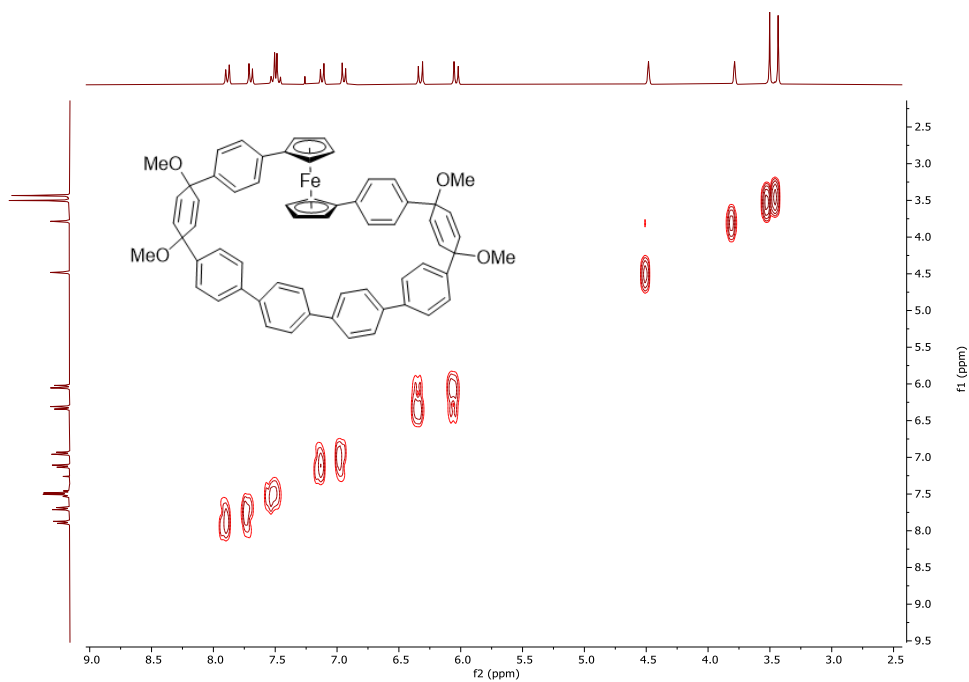
¹H-¹H COSY spectrum of compound **Fc[7]CPP** in CD₂Cl₂ (400 MHz).



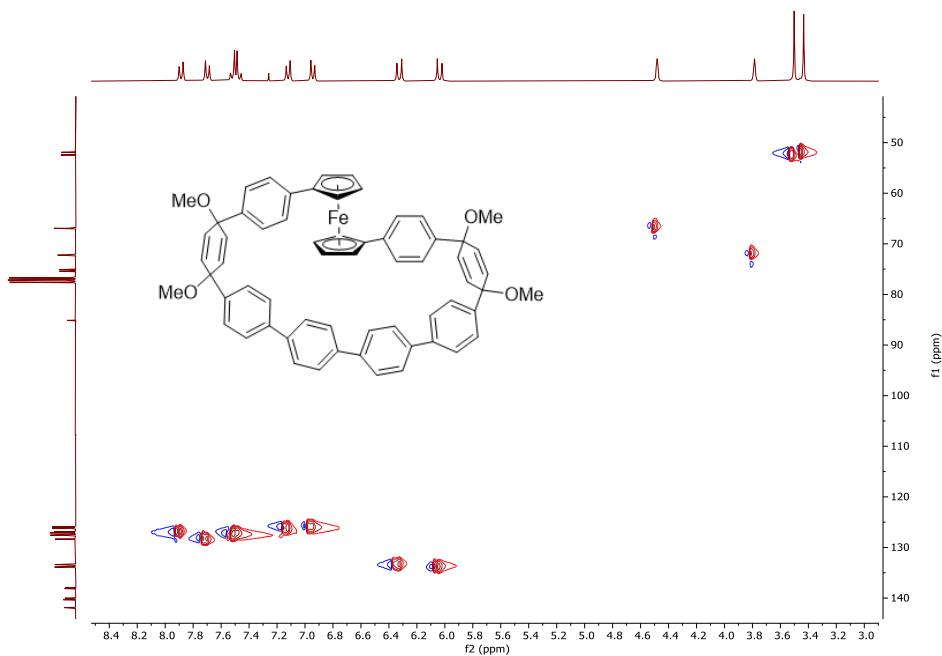
^1H - ^{13}C HSQC spectrum of compound **Fc[7]CPP** in CD_2Cl_2 (500/126 MHz).



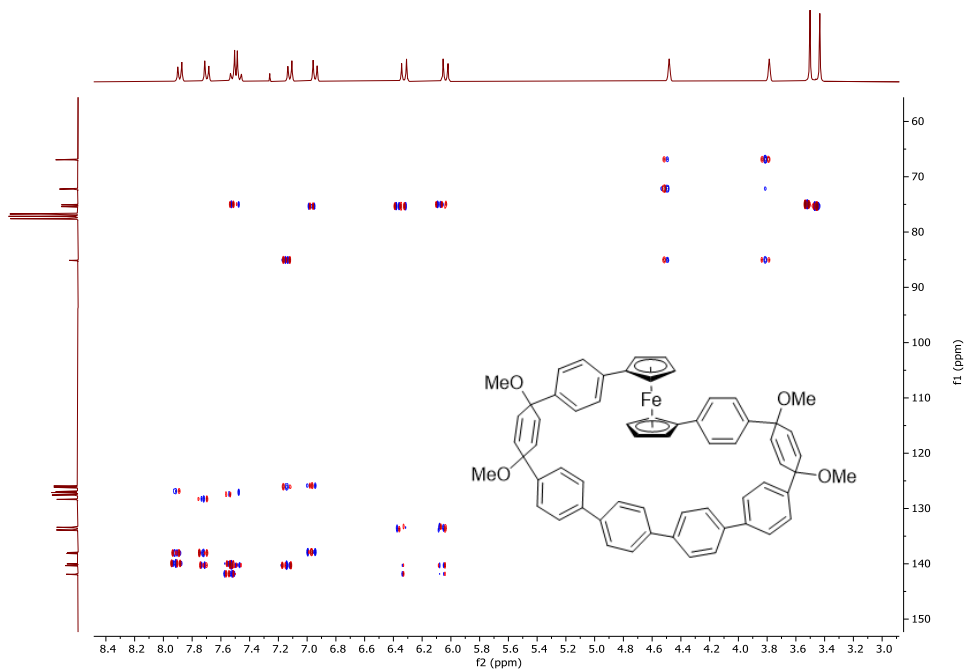
^1H - ^{13}C HMBC spectrum of compound **Fc[7]CPP** in CD_2Cl_2 (400/101 MHz).



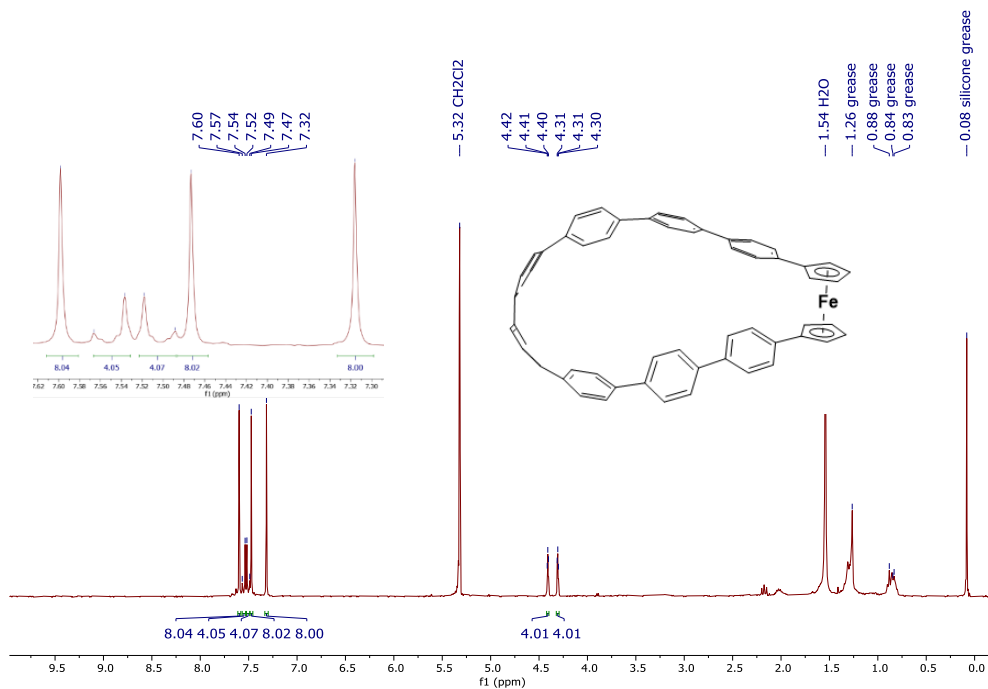
^1H - ^1H COSY spectrum of compound **pro-Fc[8]CPP** in CDCl_3 (300 MHz).



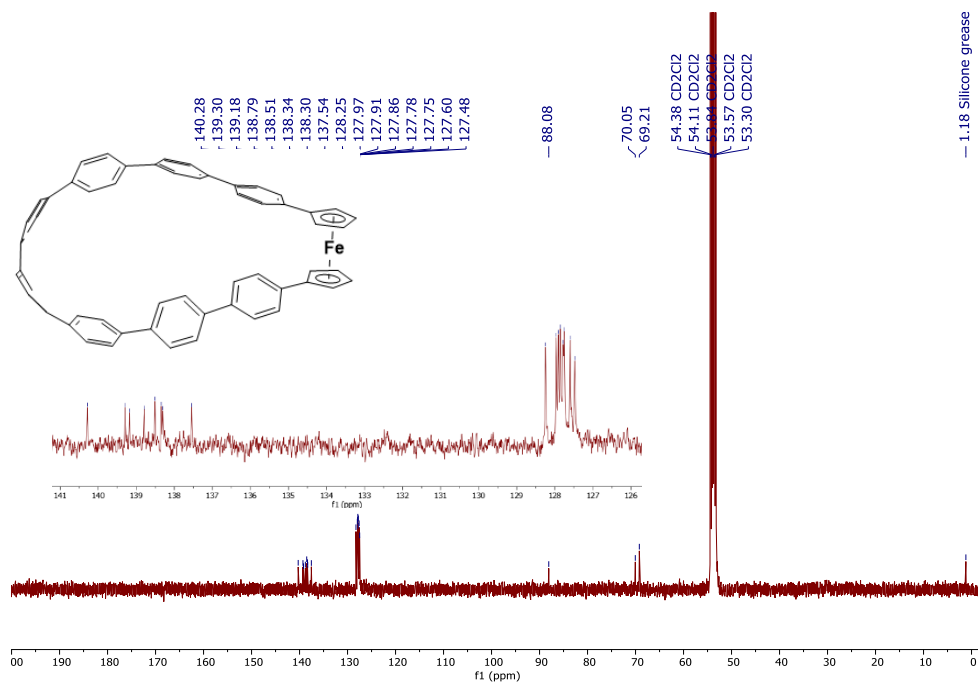
^1H - ^{13}C HSQC spectrum of compound **pro-Fc[8]CPP** in CDCl_3 (300/75 MHz).



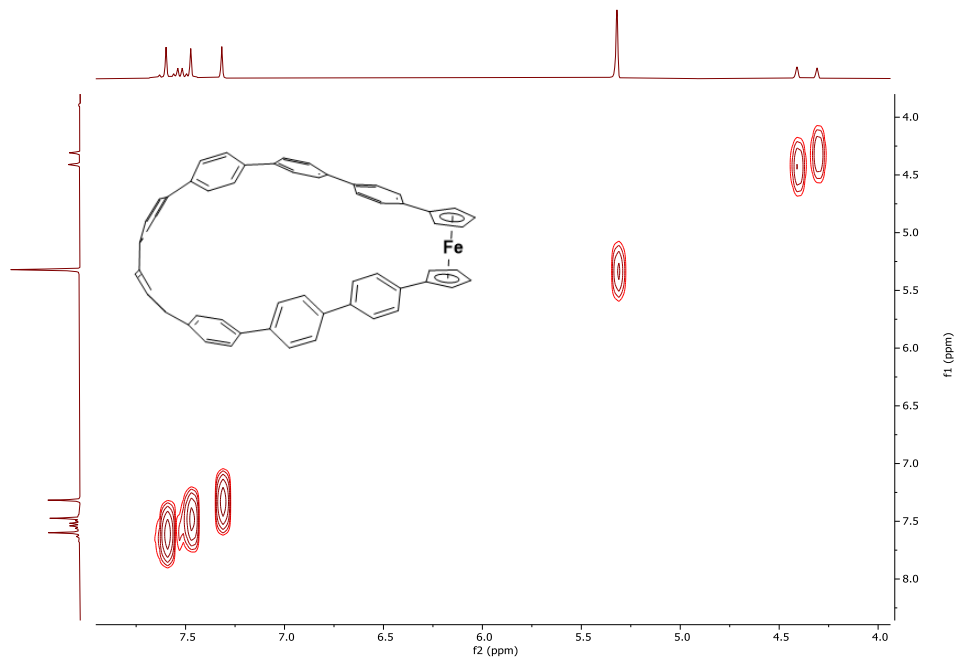
^1H - ^{13}C HMBC spectrum of compound **pro-Fc[8]CPP** in CDCl_3 (300/75 MHz).



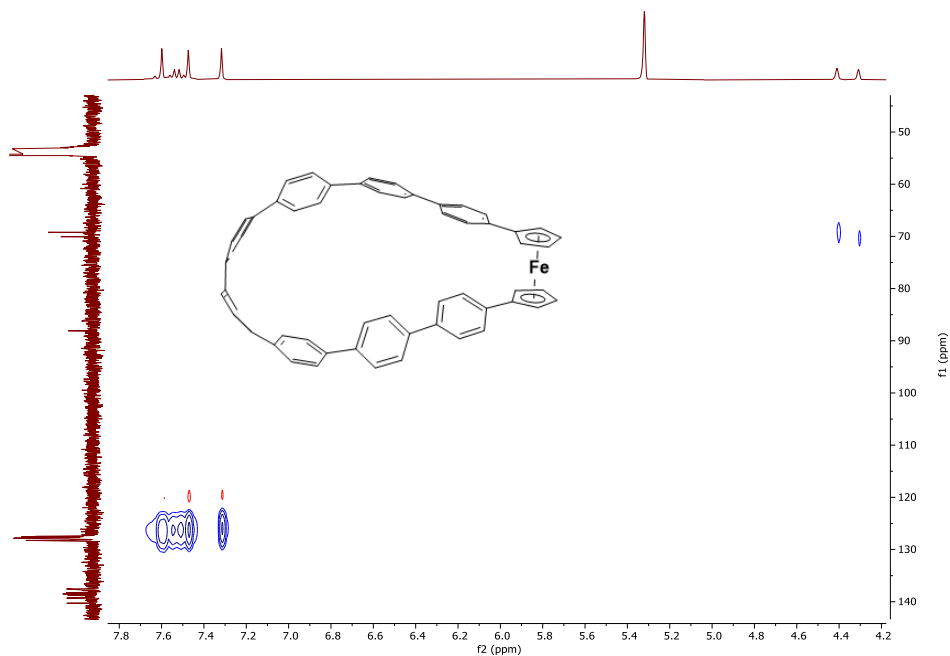
^1H NMR spectrum of compound **Fc[8]CPP** in CD_2Cl_2 (300 MHz).



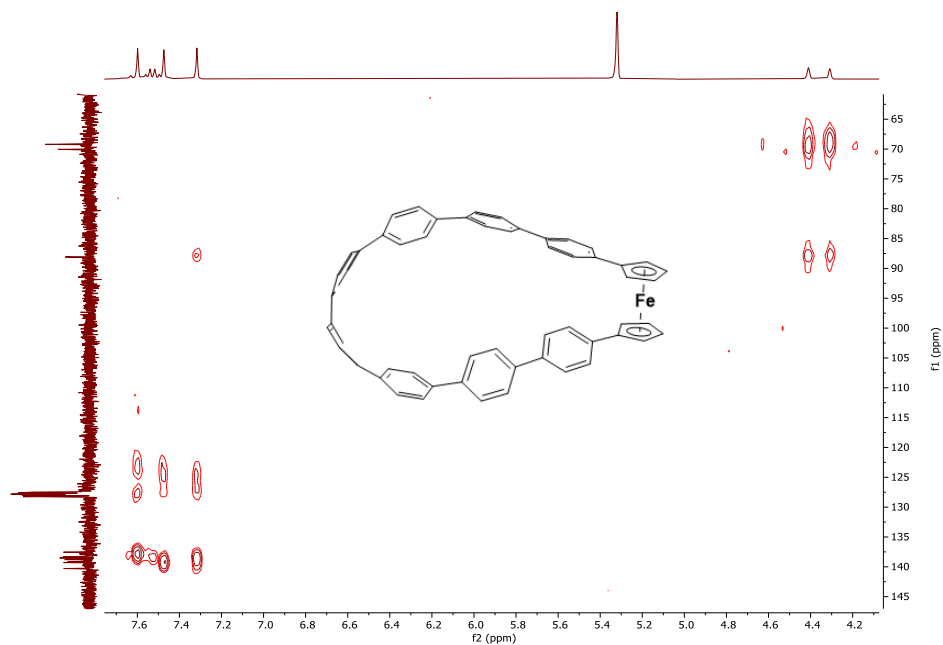
¹³C NMR spectrum of compound **Fc[8]CPP** in CD₂Cl₂ (101 MHz).



¹H-¹H COSY spectrum of compound **Fc[8]CPP** in CD₂Cl₂ (400 MHz).

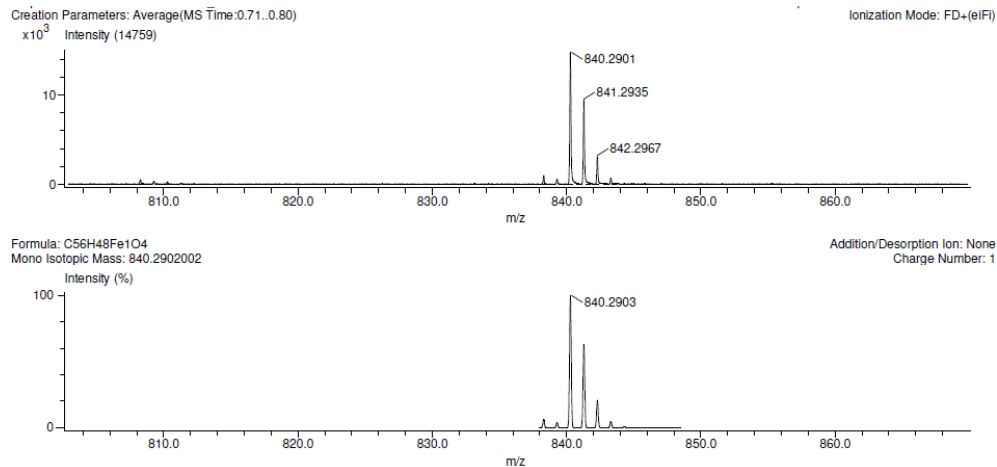


^1H - ^{13}C HSQC spectrum of compound **Fc[8]CPP** in CD_2Cl_2 (500/126 MHz).

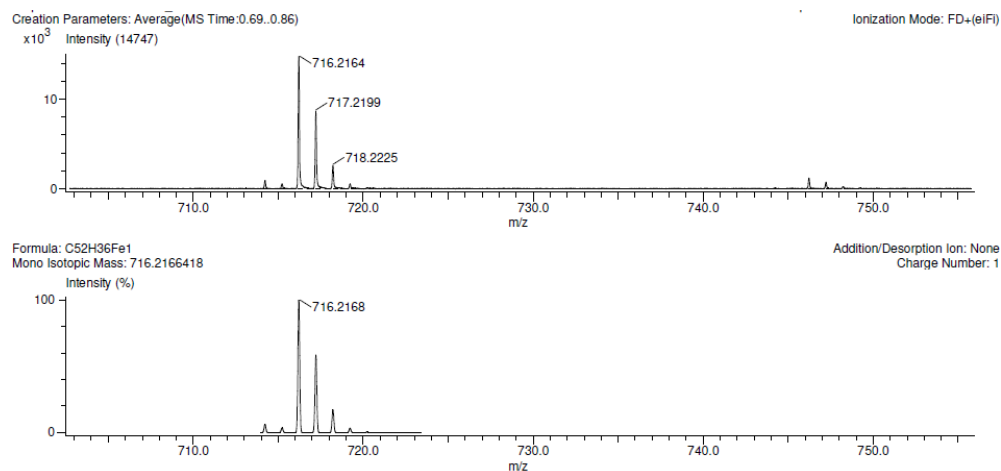


^1H - ^{13}C HMBC spectrum of compound **Fc[8]CPP** in CD_2Cl_2 (400/101 MHz).

4.4.7 Mass spectra

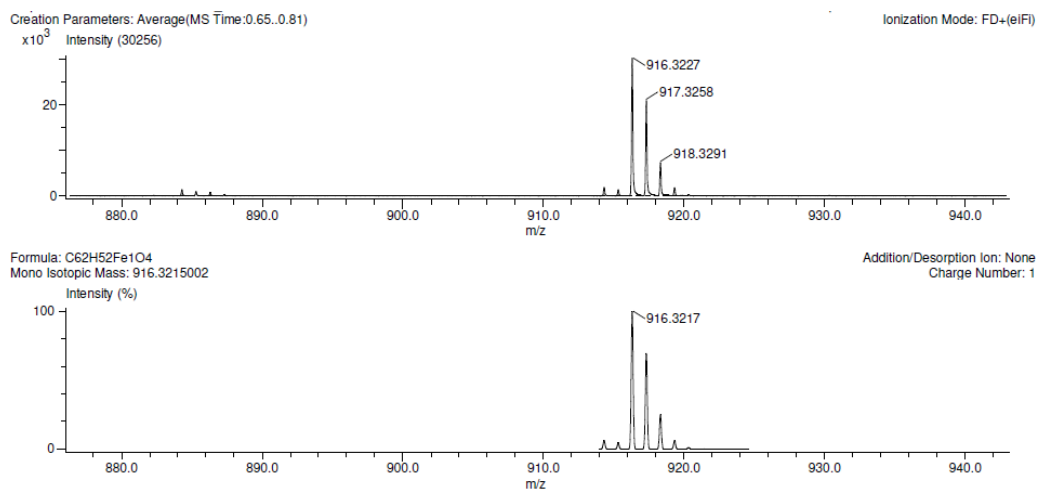


Experimental (top) and theoretical (bottom) HRMS spectra of **pro-Fc[7]CPP** (FD+).

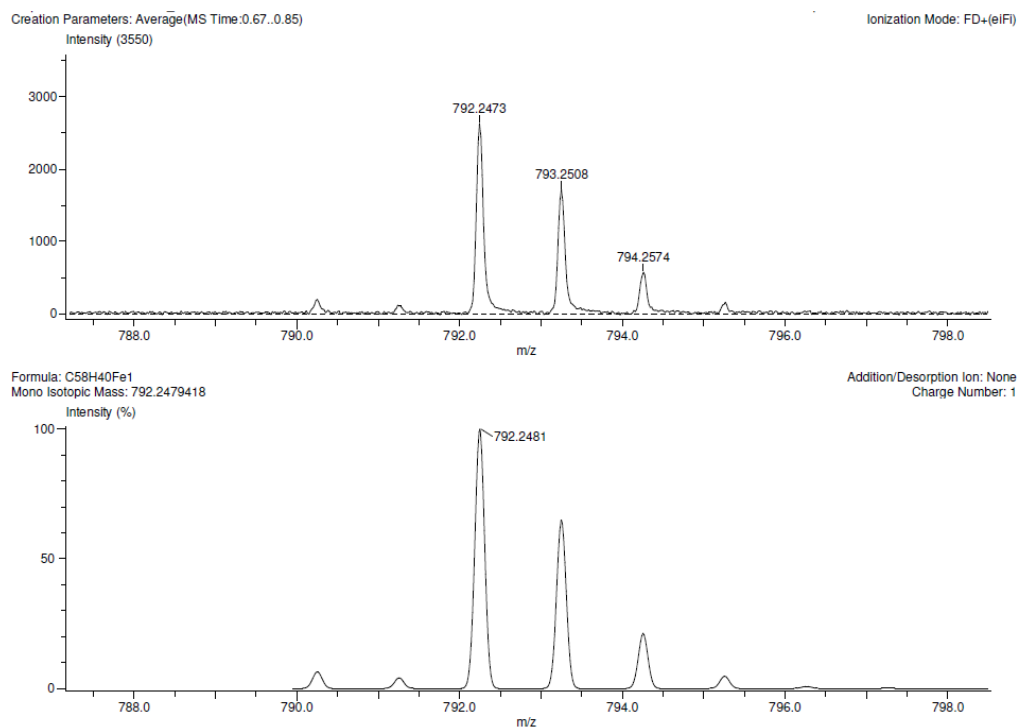


Experimental (top) and theoretical (bottom) HRMS spectra of **Fc[7]CPP** (FD+).

Chapter 4



Experimental (top) and theoretical (bottom) HRMS spectra of **pro-Fc[8]CPP** (FD+).



Experimental (top) and theoretical (bottom) HRMS spectra of **Fc[8]CPP** (FD+).

4.5 References

- [1] G. Wilkinson, M. Rosenblum, M. C. Whiting, R. B. Woodward, *J. Am. Chem. Soc.* **1952**, *74*, 2125–2126.
- [2] K. E. Lewis, G. P. Smith, *J. Am. Chem. Soc.* **1984**, *106*, 4650–4651.
- [3] L. Cunningham, A. Benson, P. J. Guiry, *Org. Biomol. Chem.* **2020**, *18*, 9329–9370.
- [4] O. Bernardo, S. González-Pelayo, L. A. López, *Eur. J. Inorg. Chem.* **2022**, *2022*, e202100911.
- [5] D. Golagani, S. Ajmeera, W. Erb, F. Mongin, S. Murthy Akondi, *Chem. Commun.* **2023**, *59*, 9259–9262.
- [6] X. Wang, Y. Qi, Y. Shen, Y. Yuan, L. Zhang, C. Zhang, Y. Sun, *Sens. Actuators B Chem.* **2020**, *310*, 127756.
- [7] R. Hein, X. Li, P. D. Beer, J. J. Davis, *Chem. Sci.* **2021**, *12*, 2433–2440.
- [8] B. Wu, S. Yeasmin, Y. Liu, L.-J. Cheng, *Sens. Actuators B Chem.* **2022**, *354*, 131216.
- [9] M.-L. Hu, M. Abbasi-Azad, B. Habibi, F. Rouhani, H. Moghanni-Bavil-Olyaei, K.-G. Liu, A. Morsali, *ChemPlusChem* **2020**, *85*, 2397–2418.
- [10] Z. Tan, H. Su, Y. Guo, H. Liu, B. Liao, A. M. Amin, Q. Liu, *Polymers* **2020**, *12*, 719.
- [11] E. Payami, A. Mohammadzadeh, K. D. Safa, R. Teimuri-Mofrad, *J. Energy Storage* **2024**, *88*, 111624.
- [12] D. Astruc, C. Ornelas, J. Ruiz Aranzaes, *J. Inorg. Organomet. Polym. Mater.* **2008**, *18*, 4–17.
- [13] G. Roy, R. Gupta, S. Ranjan Sahoo, S. Saha, D. Asthana, P. Chandra Mondal, *Coord. Chem. Rev.* **2022**, *473*, 214816.
- [14] S. Peter, B. A. Aderibigbe, *Molecules* **2019**, *24*, 3604.
- [15] A. Chaudhary, K. Poonia, *Inorg. Chem. Commun.* **2021**, *134*, 109044.
- [16] A. Berenbaum, H. Braunschweig, R. Dirk, U. Englert, J. C. Green, F. Jäkle, A. J. Lough, I. Manners, *J. Am. Chem. Soc.* **2000**, *122*, 5765–5774.
- [17] M. Tanabe, S. C. Bourke, D. E. Herbert, A. J. Lough, I. Manners, *Angew. Chem.* **2005**, *117*, 6036–6040.
- [18] T. Mizuta, Y. Imamura, K. Miyoshi, H. Yorimitsu, K. Oshima, *Organometallics* **2005**, *24*, 990–996.
- [19] E. Khozeimeh Sarbisheh, H. Bhattacharjee, M. P. T. Cao, J. Zhu, J. Müller, *Organometallics* **2017**, *36*, 614–621.
- [20] T. Mizuta, M. Onishi, K. Miyoshi, *Organometallics* **2000**, *19*, 5005–5009.
- [21] M. Tanabe, G. W. M. Vandermeulen, W. Y. Chan, P. W. Cyr, L. Vanderark, D. A. Rider, I. Manners, *Nat. Mater.* **2006**, *5*, 467–470.
- [22] D. E. Herbert, U. F. J. Mayer, J. B. Gilroy, M. J. López-Gómez, A. J. Lough, J. P. H. Charmant, I. Manners, *Chem. – Eur. J.* **2009**, *15*, 12234–12246.
- [23] R. L. N. Hailes, A. M. Oliver, J. Gwyther, G. R. Whittell, I. Manners, *Chem. Soc. Rev.* **2016**, *45*, 5358–5407.
- [24] M. Di Giannantonio, M. A. Ayer, E. Verde-Sesto, M. Lattuada, C. Weder, K. M. Fromm, *Angew. Chem. Int. Ed.* **2018**, *57*, 11445–11450.
- [25] Y. Sha, Y. Zhang, E. Xu, Z. Wang, T. Zhu, S. L. Craig, C. Tang, *ACS Macro Lett.* **2018**, *7*, 1174–1179.
- [26] Y. Zhang, Z. Wang, T. B. Kouznetsova, Y. Sha, E. Xu, L. Shannahan, M. Fermen-Coker, Y. Lin, C. Tang, S. L. Craig, *Nat. Chem.* **2021**, *13*, 56–62.
- [27] P. Aisen, C. Enns, M. Wessling-Resnick, *Int. J. Biochem. Cell Biol.* **2001**, *33*, 940–959.
- [28] C. Furdui, S. W. Ragsdale, *Biochemistry* **2002**, *41*, 9921–9937.

- [29] C. Hsiao, I.-C. Chou, C. D. Okafor, J. C. Bowman, E. B. O'Neill, S. S. Athavale, A. S. Petrov, N. V. Hud, R. M. Wartell, S. C. Harvey, L. D. Williams, *Nat. Chem.* **2013**, *5*, 525–528.
- [30] P. Ponka, *Kidney Int.* **1999**, *55*, S2–S11.
- [31] W. A. Eaton, E. R. Henry, J. Hofrichter, A. Mozzarelli, *Nat. Struct. Biol.* **1999**, *6*, 351–358.
- [32] D. J. Livingston, W. D. Brown, *FOOD Technol.* **1981**.
- [33] J. Liu, S. Chakraborty, P. Hosseinzadeh, Y. Yu, S. Tian, I. Petrik, A. Bhagi, Y. Lu, *Chem. Rev.* **2014**, *114*, 4366–4469.
- [34] R. C. Blake II, E. A. Shute, M. M. Greenwood, G. H. Spencer, W. J. Ingledew, *FEMS Microbiol. Rev.* **1993**, *11*, 9–18.
- [35] P. Nordlund, P. Reichard, *Annu. Rev. Biochem.* **2006**, *75*, 681–706.
- [36] I. De Domenico, D. McVey Ward, J. Kaplan, *Nat. Rev. Mol. Cell Biol.* **2008**, *9*, 72–81.
- [37] A. Pietrangelo, C. Trautwein, *Nat. Clin. Pract. Gastroenterol. Hepatol.* **2004**, *1*, 39–45.
- [38] D. Galaris, A. Barbouti, K. Pantopoulos, *Biochim. Biophys. Acta Mol. Cell Res.* **2019**, *1866*, 118535.
- [39] O. Marques, G. Weiss, M. U. Muckenthaler, *Blood* **2022**, *140*, 2011–2023.
- [40] R. B. Kręćjasz, J. Malinčík, S. Mathew, P. Štacko, T. Šolomek, *J. Am. Chem. Soc.* **2025**, *147*, 10231–10237.
- [41] R. Jasti, J. Bhattacharjee, J. B. Neaton, C. R. Bertozzi, *J. Am. Chem. Soc.* **2008**, *130*, 17646–17647.
- [42] Y. Segawa, A. Yagi, K. Matsui, K. Itami, *Angew. Chem. Int. Ed.* **2016**, *55*, 5136–5158.
- [43] T. Mizuta, M. Onishi, K. Miyoshi, *Organometallics* **2000**, *19*, 5005–5009.
- [44] R. Sievers, N. Hartmann, P. S. Riemann, T.-N. Streit, M. Malischewski, *Chem. Sci.* **2025**, DOI 10.1039/D5SC02784E.
- [45] R. Sievers, N. G. Kub, T.-N. Streit, M. Reimann, G. Thiele, M. Kaupp, M. Malischewski, *Angew. Chem. n.d.*, *n/a*, e202505783.
- [46] V. K. Patel, E. Kayahara, S. Yamago, *Chem. – Eur. J.* **2015**, *21*, 5742–5749.
- [47] T. C. Lovell, C. E. Colwell, L. N. Zakharov, R. Jasti, *Chem. Sci.* **2019**, *10*, 3786–3790.
- [48] P. J. Evans, E. R. Darzi, R. Jasti, *Nat. Chem.* **2014**, *6*, 404–408.
- [49] T. Iwamoto, Y. Watanabe, Y. Sakamoto, T. Suzuki, S. Yamago, *J. Am. Chem. Soc.* **2011**, *133*, 8354–8361.
- [50] E. Kayahara, K. Fukayama, T. Nishinaga, S. Yamago, *Chem. – Asian J.* **2016**, *11*, 1793–1797.
- [51] Y. Segawa, H. Omachi, K. Itami, *Org. Lett.* **2010**, *12*, 2262–2265.
- [52] T. Iwamoto, Y. Watanabe, Y. Sakamoto, T. Suzuki, S. Yamago, *J. Am. Chem. Soc.* **2011**, *133*, 8354–8361.
- [53] E. R. Darzi, R. Jasti, *Chem. Soc. Rev.* **2015**, *44*, 6401–6410.
- [54] E. Kayahara, T. Iwamoto, T. Suzuki, S. Yamago, *Chem. Lett.* **2013**, *42*, 621–623.
- [55] J. Xia, R. Jasti, *Angew. Chem. Int. Ed.* **2012**, *51*, 2474–2476.
- [56] P. Li, T. J. Sisto, E. R. Darzi, R. Jasti, *Org. Lett.* **2014**, *16*, 182–185.
- [57] P. Li, T. J. Sisto, E. R. Darzi, R. Jasti, *Org. Lett.* **2014**, *16*, 182–185.
- [58] E. R. Darzi, T. J. Sisto, R. Jasti, *J. Org. Chem.* **2012**, *77*, 6624–6628.
- [59] Y. Segawa, A. Fukazawa, S. Matsuura, H. Omachi, S. Yamaguchi, S. Irle, K. Itami, *Org. Biomol. Chem.* **2012**, *10*, 5979.
- [60] S. Scuppa, L. Orian, D. Dini, S. Santi, M. Meneghetti, *J. Phys. Chem. A* **2009**, *113*, 9286–9294.
- [61] M. Yáñez-S, S. A. Moya, C. Zúñiga, G. Cárdenas-Jirón, *Comput. Theor. Chem.* **2017**, *1118*, 65–74.

- [62] M. M. Flores-Leonar, R. Moreno-Esparza, V. M. Ugalde-Saldívar, C. Amador-Bedolla, *Comput. Theor. Chem.* **2017**, *1099*, 167–173.
- [63] M. Toma, T. Kuvék, V. Vrček, *J. Phys. Chem. A* **2020**, *124*, 8029–8039.
- [64] Bruker, SAINT V8.40B, Bruker AXS Inc., Madison, Wisconsin, USA, **2001**.
- [65] L. Krause, R. Herbst-Irmer, G. M. Sheldrick, D. Stalke, *J. Appl. Crystallogr.* **2015**, *48*, 3–10.
- [66] G. M. Sheldrick, *Acta Crystallogr. Sect. Found. Adv.* **2015**, *71*, 3–8.
- [67] A. L. Spek, *J. Appl. Crystallogr.* **2003**, *36*, 7–13.
- [68] G. M. Sheldrick, *Acta Crystallogr. Sect. C Struct. Chem.* **2015**, *71*, 3–8.